



Article

A Correlation Between Earthquake Magnitude and Pre-Seismic Gravity Field Variations over Its Epicenter

Chrysanthi Chariskou D, Eleni Vrochidou * and George A. Papakostas

MLV Research Group, Department of Informatics, Democritus University of Thrace, 65404 Kavala, Greece; chcharis@cs.duth.gr (C.C.); gpapak@cs.duth.gr (G.A.P.)

* Correspondence: evrochid@cs.duth.gr; Tel.: +30-2510-462320

Abstract

Earthquakes are the result of complex interactions between tectonic plates, the mantle, and the lithosphere. Complex geodynamic conditions contribute to the occurrence of seismic phenomena. Tectonic plates can collide, move apart, or slide past each other. Mantle convection by internal heat drives plate motions that deform the lithosphere. Rocks deform elastically as stress accumulates and pore fluid pressure changes. Rupture occurs when stress exceeds frictional resistance. The connection between variations in gravity and the magnitude of earthquakes remains unclear. This work aims to examine aspects of this correlation. Three sets of earthquakes, one with events from all over the world, one from broader Greece, and one from the Hellenic Trench in Greece, aiming to cover all cases of geodynamics, from very different to very similar, were employed. Time series of gravity measurements at earthquake epicenters were extracted from GRACE satellite data. Time derivatives of the gravity field, as well as magnitude-dependent variations—reflecting changes relative to earthquake strength—were computed. Multiple linear regression (MLR), partial least squares (PLS) regression, and neural networks (NN) were used to model the relationship between gravity or its derivatives and earthquake magnitude. A correlation between the earthquake magnitude and magnitude derivatives was found. By using the global and Greek datasets, the best accuracy was obtained with MLR, reporting a mean squared error (MSE) of 0.069 with an R² of 0.979, and MSE was 0.011 with R² score of 0.997, respectively. By using the Hellenic Trench set, PLS regression derived the best correlation results, reporting an MSE of 0.004 and an R² of 0.977. Experimental results suggest that gravity, and therefore crustal density, is related to the magnitude of the impending earthquake, but not to its timing.

Keywords: gravity; earthquake; lithosphere; machine learning; magma; MLR; neural network; PLS; satellite image



Academic Editors: Ester Piegari, Stefania Gentili and Andrea Carpinteri

Received: 25 August 2025 Revised: 23 September 2025 Accepted: 15 October 2025 Published: 17 October 2025

Citation: Chariskou, C.; Vrochidou, E.; Papakostas, G.A. A Correlation Between Earthquake Magnitude and Pre-Seismic Gravity Field Variations over Its Epicenter. *Appl. Sci.* **2025**, *15*, 11126. https://doi.org/10.3390/app152011126

Copyright: © 2025 by the authors. Licensee MDPI, Basel, Switzerland. This article is an open access article distributed under the terms and conditions of the Creative Commons Attribution (CC BY) license (https://creativecommons.org/licenses/by/4.0/).

1. Introduction

Earthquakes are among the most devastating natural disasters. Predicting the occurrence and magnitude of earthquakes has long been a subject of scientific research [1,2]. Prediction of earthquake occurrence or magnitude is based on the detection and monitoring of certain seismic precursor geophysical events occurring at various distances around the epicenter of the earthquake [3–5]. These seismic precursor signs include electromagnetic perturbations of ultra-low frequency (ULF) and very low frequency (VLF) [6–9], gravity changes [10–13], vertical and lateral ground movements [14–17], alterations in groundwater level, its chemical composition, and its temperature [18–21], emission of hydrogen,

carbon dioxide, and radon gases [22–24], the occurrence of swarms of lower magnitude earthquakes before the main one [25,26], and changes in characteristics of the atmosphere over the imminent earthquake epicenter, such as atmospheric heat and density, ionosphere electron content, and atmospheric cation (H⁺, O⁺ and He⁺) content.

The study of gravity perturbations as potential seismic precursors has a long history in earthquake research. Pre-seismic gravity fluctuations have been recorded around the site of an imminent earthquake in many cases [11,13,27–34]. Early observations date back to the 1960s. Barnes (1966) [35] documented gravity variations associated with the 27 March 1964, Alaska earthquake, while Fujii (1966) [36] reported both pre-seismic and post-seismic gravity anomalies related to the Niigata earthquake of 16 June 1964, in Japan. Between 1967 and 1971, similar gravity changes were also recorded related to other earthquakes [37–39]. Various mechanisms were proposed to explain these phenomena: Kisslinger (1975) [38] attributed gravity changes to horizontal dilatancy of subsurface layers and inflow of groundwater into fractures; Barnes (1966) [35] suggested mass displacements, whereas Oliver et al. (1975) [39] argued that both crustal deformation and surface movements could account for the observed gravity disturbances.

Research on pre-seismic gravity variations continued over the following three decades. Chen Yun-Tai et al. (1979) [40] found that gravity decreased in areas surrounding the 4 February 1975, Haicheng earthquake but increased before the 28 July 1976, Tangshan earthquake, both in China. Their analysis outlined mass redistribution as the most plausible explanation. Similarly, Hagiwara (1979) [41] reported pre-seismic gravity anomalies preceding three Chinese earthquakes between 1975 and 1976. During that period, significant efforts were directed toward modeling the relationship between gravity changes and seismic activity, with approaches incorporating dilatancy, deep fluid migration, and dip-slip faulting models of crustal deformation [42–46]. Until recently, these studies relied mainly on terrestrial gravimeters; however, since 2020, satellite-based gravity measurements have also been employed [11,12,27,47].

In addition to precursor studies, it has been shown that rapid mass redistribution during large earthquake ruptures produces so-called Prompt Elasto-Gravity Signals (PEGS) [48,49]. These signals propagate at the speed of light and can be detected seconds before seismic waves arrive at distant locations. While PEGS may provide useful constraints on the magnitude of very large earthquakes, they are not considered true precursor signals, since they are generated concurrently with the rupture process.

There is still no agreement regarding the underlying reasons for the local disturbances detected in gravity. Most of the related theories are cited by Liu et al. [50] and Zhu et al. [34]. According to the proposed models, the rocks are expanding under the stress imposed on them before the earthquake, and cracks are created in the lithosphere, causing changes in the average crustal mass density, with or without aqueous fluid insurgence from deep crustal sources, and therefore changes in the local gravity are observed. According to the lithospheric plate dislocation model, it is the release of stress at the points of contact of the continuously moving plates that causes the cracks. There is evidence that the change in the weight of ice masses over polar regions, as the ice melts, could trigger earthquakes [51]. But there is also evidence of magma movements as the causal factor of earthquake generation, at least in regions close to volcanoes [29,32,52,53]. Whatever the causes of gravity changes, there is undisputable published evidence that they constitute pre-seismic signals of incoming earthquakes [13,28–34]. In only a few cases, the gravity changes were measured by satellites [12,27,47,53]. In the majority of the published work, the gravity was recorded using ground-based gravimeters [12,27,47]. Prediction of earthquake occurrence or magnitude using gravity data is still far from satisfactory. In one of the most successful efforts, Zhu et al. [34] used an extensive network of terrestrial gravimeters all over China to predict

the epicenter and year of occurrence of 13 earthquakes of surface wave magnitude (M_s) only between 6 and 7 degrees M_s . They measured the gravity change intensity in a time series and its variation trend. Note that the M_s scale is logarithmic, like the Richter scale, and is designed to give similar numerical results, especially towards the middle values. The authors attribute the limitations in the prediction range to restrictions in the accuracy of the gravity meters and their coordination in the network, the unforeseen underground water and mass movements, and the fluctuating nature of the gravity magnitudes over time.

To this end, the objective of this work is to investigate and establish a more comprehensive relation between the gravity change intensities and the magnitudes of various earthquakes selected from all over the world, covering a broad range of geodynamics, from very different to very similar. The fluctuating nature of the gravity readings indicates either wave-like up and down movements of solid and semi-solid masses under the lithosphere or cyclical opening and resealing of lithospheric cracks. A way was sought to relate these cyclical changes, rather than the absolute gravity reading, to the earthquake magnitudes. Satellite-recorded gravity data over the epicenter of a list of worldwide earthquakes were used for this study. The gravity data were used by Python 3.11.13 algorithms run in the Jupiter Notebook environment of the Anaconda graphical user interface. Multiple linear regression (MLR) and partial least squares (PLS) regression methods were used as described before [54] to correlate earthquake magnitudes with the gravity values or their derivatives. A neural network (NN) algorithm was also implemented. It was found that a close relation exists between the derivatives of pre-existing gravity values over the epicenter of the earthquakes and the earthquake magnitude. This information holds a promising potential for integration into feature fusion techniques; by combining gravity derivatives with other relevant predictors, we can enhance the accuracy and robustness of artificial intelligence (AI) earthquake magnitude prediction models as a warning for natural disaster prevention, leveraging the complementary strengths of multiple data sources.

The rest of the paper is structured as follows: Section 2 presents materials and proposed methods. Results are summarized in Section 3, while discussions and conclusions are included in Sections 4 and 5, respectively.

2. Materials and Methods

2.1. Proposed Methodology

A block diagram of the steps followed for the examination of the correlation of an earthquake's magnitude to gravity is given in Figure 1. Three earthquake datasets were constructed, one including earthquakes from all over the world, one including earthquakes from Greece and its close neighborhood, and one targeted on the Hellenic Trench in Greece. The global dataset consisted of 25 earthquakes with magnitudes between 1.0 and 7.3, the Greek dataset consisted of 26 earthquakes with magnitudes between 2.7 and 7.0, while the Hellenic Trench dataset consisted of 12 earthquakes of magnitudes 5.0 to 6.5.

The Greek dataset was employed due to the fact that the particular geodynamics of distant localities on Earth can vary to a large extent, and this might theoretically affect the association of gravity anomaly values with the earthquake magnitude. The Greek dataset refers to a much more confined geographic area, and, therefore, it is expected to have more homogeneous geodynamics. Towards the same direction, the Hellenic Trench dataset aims to test earthquakes of an even higher geodynamic homogeneity. The Hellenic Trench, also referred to as the Hellenic Arc or Hellenic Conduction Zone area, is a convergent plate boundary where the African Plate is sliding beneath the Aegean microplate. This boundary is a narrow arc starting from the Ionian Sea in the west, passing south of the island of Crete and rising again towards the Dodecanese Islands in the east. The earthquakes occurring at this boundary are interplate thrust Earthquakes [55–58].

Appl. Sci. 2025, 15, 11126 4 of 26

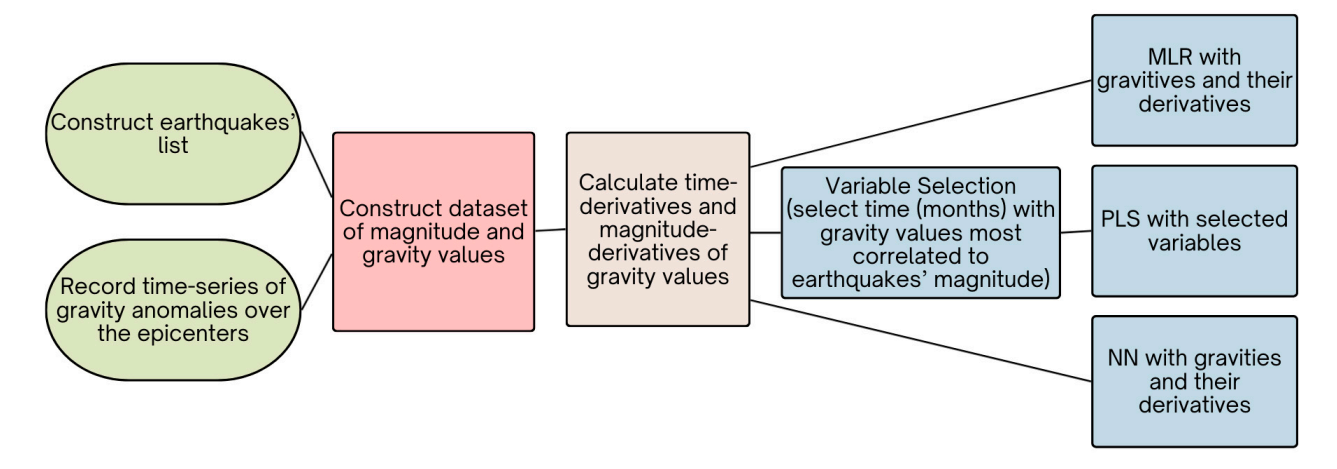


Figure 1. Proposed methodology.

For the global dataset, a time series of gravity anomaly values at their epicenter was also recorded for the day closest to the earthquake and for each of the nine consecutive months before this measurement. For the Greek dataset, the gravity anomaly values were recorded for five 10-day intervals, starting nine months before the earthquake and ending with a final measurement as close as possible to the earthquake date.

It should be noted here that, since in this work we are analyzing the derivatives of the gravity values G with respect to the earthquake magnitudes M, the latter implies that G is a continuous function of M. Therefore, it is considered necessary that M consistently refers to the same physical quantity. For this reason, in case of magnitude values less than 5, referring to the global and the Greek datasets, which were recorded in the mb, ml, md, or mwr scales, these values were converted to the mww scale, which is the scale used in case of magnitudes over 5.0, by employing widely accepted conversion formulas [59,60].

Since the dataset of global earthquakes is formed from earthquakes from all over the world, it is important to examine whether the local geodynamics would influence the correlation between the magnitude of the earthquakes and the gravity anomaly values or their derivatives. A more confined geographic area would answer the argument that different geodynamics of the earthquakes make them unsuitable for comparison. In addition, the time span of gravity measurements was shortened in the Greek dataset to only 50 days, five measurements at 10-day intervals, ending on a day as close as possible to the day of the earthquake. This limits the possibility of large changes in geodynamics in Greece during the 50-day interval of gravity measurements. In the Hellenic Trench dataset, the similarity of earthquake types is ensured to an even more significant degree, not only due to the limited geographic extent but primarily because of the uniform geodynamic characteristics.

Based on these data, the final datasets were then constructed, containing the earth-quake magnitudes and the recorded gravity values. The derivatives along months were calculated and are referred to in this text as time derivatives. Magnitude derivatives, showing the change in gravity as the earthquake magnitude changes, were also calculated.

Finally, gravity values and their derivatives were separately fed into MLR, PLS, and NN algorithms to infer any connection between magnitude and gravity from the magnitude prediction accuracy of the prediction models. For improved prediction of the PLS model, variable selection was applied by selecting the months of the dataset whose gravity and derivative values produced the lowest mean squared error (MSE).

2.2. Construction of Earthquake Datasets

In this work, earthquakes were selected from all over the world and in Greece using the United States Geological Survey Search Comprehensive Earthquake Catalogue (USGS Appl. Sci. **2025**, 15, 11126 5 of 26

Earthquake Hazards Program) [61,62]. It should be noted here that the aim of this work is not to examine the geodynamic details of earthquakes but to look for a common factor among many earthquakes that have different geodynamic substrates. In the case of the global dataset, the earthquakes are purposely selected from widespread areas so as to minimize the influence of local geodynamic conditions. The latter approach is an effort to investigate the common gravity-related denominator related to their magnitude, irrespective of the local geological peculiarities. The mechanism of earthquake induction could be different, yet the accompanying gravity conditions still exist. Moreover, a close time window was selected to neutralize as far as possible the external factors, such as lunar and solar gravity effects.

Thus, the following datasets of earthquakes were constructed: the global dataset, which comprised 25 earthquakes that occurred in May of 2021; the Greek dataset comprised 26 earthquakes that occurred during the year 2020; and the Hellenic Trench dataset, which comprised 12 earthquakes of the same geodynamics. For this work, gravity anomaly is defined as the deviation (in μ Gal) of the mean monthly gravity value at the earthquake (epicenter) from the long-term mean gravity value, calculated over the six-year reference period between January 2004 and December 2009. More details on both datasets are provided in Tables A1 and A2 in the Appendix A section.

This research relies on gravity observations from the GRACE mission, a joint initiative between NASA and the German Aerospace Center (DLR), implemented through its twin satellites GRACE-1 and GRACE-2, available at https://earthquake.usgs.gov/earthquake/search/ (assessed on 11 September 2025). The datasets are archived within the GFZ Data Services Sample catalog, maintained by the Helmholtz Center for Geosciences in Brandenburg [63]. For the purposes of this study, processed gravity solutions were obtained via the COST-G Plotter [64]. COST-G, operating under the International Combination Service for Time-Variable Gravity Fields and linked to the International Gravity Field Service (IFS), combines individual monthly gravity field solutions into an internally consistent global model. Time series of gravity anomalies (reported in mGAL) at the central locations of the selected earthquakes were extracted from the GFZ repository [63]. For monthly data visualization, the RL06.1 DDK5 product of COST-G was employed, which represents gravity field variations using GPS-based coordinates of the earthquake epicenters, while for 10-day intervals, the collection CNES RLO5 TSVD (10-day) was used.

It should be noted here that GRACE satellite gravity sensors suffer from attenuation or leakage bias of the gravity signal, meaning that the induced filtering smooths out the noise but also may weaken the actual gravity signal. The latter issue is avoided by employing spatial filtering of the gravity data. Our data come from the GFZ RL06.1 DDK5 dataset in the COST-G Plotter, which employs spatial filtering to reduce noise and leakage bias. The DDK filters (decorrelation and smoothing filters) are performing exactly this; they have various ratios of noise suppression to preserve spatial details. The DDK5 is a compromise-level filter.

2.3. Data Processing and Machine Learning

The earthquake dataset was saved in the Jupyter Notebook v6.3 as an .xlsx file. A summary of the data processing and the algorithm characteristics is given in Table 1. The column containing the magnitudes of the earthquakes was separated and transformed into a one-dimensional array. The gravity values were formulated into a two-dimensional array and were standardized by scaling to unit variance. The Savitzky–Golay filter was implemented to calculate the first- and second-order derivatives of the gravity values. The first-order time derivatives show the speed of gravity changes as the time of the earthquake occurrence is approached. The second derivatives are the accelerations; the

rate of change in the speed of gravity changes as the time of the earthquake is approached. Magnitude derivatives, showing the rate and acceleration of gravity changes as we move along the earthquake magnitudes, were also estimated. Their physical meaning is the correlation between the magnitude of the earthquake and any pre-existing geophysical factors determining the gravity magnitude at the site of the earthquake, irrespective of time-related gravity changes. For MLR, the magnitude and gravity sets were split into training and test sets, with thirty percent of the earthquakes used for testing the regression model performance. For NN, the best prediction results were produced with a test set size of twenty percent.

Table 1. Data processing and algorithm characteristics.

Data Processing	MLR	PLS Regression	Neural Network
Data scaling by using the Standard scaler () function of the Scikit-learn 1.7.1 library. Calculation of derivatives by using the SavgolFilter () function of the Scipy 1.16.1 library. Calculation of the slope of gravity values through the months, by using the LinearRegression.fit () function of the Scikit-learn 1.7.1 library.	Used as callable function. Regression: linear. Test size: 0.3 Performance metrics: MSE, R ² score. Plotting predicted against actual magnitudes.	Used as callable function Number of components: The optimal determined by variable selection. Model regression function: PLS regression Metrics for evaluation of model performance and prediction: MSE, R ² score Plotting predicted against actual magnitudes	Used as callable function. Keras 3.10.0 model: sequential, regression. Test size: 0.2 Input shape: 10 Input layer: 10 nodes, activation: relu Hidden layers: one layer of three nodes, activation: relu Output layer: one node, activation: linear 200 epochs, batch size: 3 Performance metrics: MSE, R ² score Plotting predicted against actual magnitudes

Variable selection refers to the selection of those columns (variables) from the gravity or gravity derivative datasets that produce the least MSE of magnitude prediction using PLS regression. A Python algorithm was formulated for variable selection, described in Chariskou et al. [54].

The neural network was a Keras 3.10.0 regression net. The input layer of the neural network model had as input shape the number of columns of the tested gravity data and also ten neural nodes. One hidden layer of three nodes and activation 'relu' followed. The output layer had one node and activation 'linear', as suggested for regression models. Two hundred passes (epochs) of the entire set of rows were used, and weights were recalculated after every three-row pass (batch size). The algorithm is splitting the gravity and earthquake magnitude sets into train and test sets (80–20%), calculating the MSE and R^2 score between the actual and predicted magnitudes, and plotting them.

3. Results

3.1. Results on the Global Dataset

In Table 2, the gravity anomaly values for the set of global earthquakes are presented, consisting of 25 earthquakes. The monthly gravity anomaly values at a variable time (last column, depending on the available data in the COST-G Plotter) from the days before the occurrence of the earthquake up to nine months before this last measurement were recorded. The magnitude spans a range of earthquake magnitudes from 1.0 to 7.3.

Table 2. The magnitude (mag) and gravity anomaly values over the earthquake epicenter on the first day closest to the day of the earthquake ('last measurement') and for each of the nine months before that last measurement. The time lag between the day of the earthquake and the last measurement of gravity anomaly is given in the column 'days after last measurement' and depends on the available data in the COST-G Plotter gravity database.

			C	Gravity Anon	naly (µGal) B	efore the Ear	rthquake Occ	currence			D 46 I .
Mag	9 Months	8 Months	7 Months	6 Months	5 Months	4 Months	3 Months	2 Months	1 Month	Last Measurement	Days After Last Measurement
1.57	-3.487	-5.937	-4.278	-4.369	-1.289	-3.520	-1.749	-4.532	-5.786	-2.765	4
2.24	-4.138	-4.108	-2.820	-3.337	-0.600	-4.086	-3.067	-1.144	-1.055	-1.535	15
3.15	-1.034	-0.426	0.364	0.614	-1.279	1.061	1.197	-0.086	-1.932	0.854	25
3.81	0.056	3.094	2.305	-0.931	-1.231	1.719	3.018	1.632	2.674	0.022	8
3.92	2.037	0.632	2.405	1.711	4.630	1.980	2.967	0.818	-0.591	3.452	11
4.38	-5.344	-5.530	-6.569	-3.466	-3.616	0.480	-1.455	-2.676	-2.694	1.791	15
4.49	2.777	1.443	2.865	2.702	2.388	-0.754	1.278	-0.077	2.233	1.667	15
4.60	-1.349	0.794	1.304	0.276	1.835	-2.168	3.664	2.941	3.101	0.715	29
4.71	-0.035	3.146	2.384	-0.854	-1.071	1.737	3.107	1.705	2.794	0.102	11
4.82	6.548	5.996	4.717	3.617	4.899	4.233	4.752	4.362	7.393	5.855	4
4.93	-5.026	-5.050	-4.505	-5.224	-1.393	-4.778	-1.554	0.512	4.305	-1.561	11
5.10	-4.883	-0.989	-2.268	-1.282	-0.539	-1.495	0.799	-0.655	0.856	-0.549	15
5.20	-0.739	-1.745	-0.400	-1.701	-3.591	-4.291	-3.604	-0.037	-3.262	-0.828	4
5.30	0.181	-3.431	-0.853	0.221	-1.784	-1.306	0.347	-0.111	-0.933	-0.341	18
5.40	1.187	-0.334	1.644	1.786	1.259	0.978	0.387	2.953	1.942	1.578	4
5.50	10.093	10.243	9.949	10.278	13.981	9.739	9.423	8.840	9.917	6.484	14
5.60	3.130	-0.102	0.223	1.814	-0.386	0.390	0.583	0.014	-0.552	-1.204	15
5.70	-0.159	-0.092	2.888	0.080	0.945	2.912	1.728	1.169	1.571	1.153	8
5.80	1.452	1.319	-1.649	-1.760	-1.215	0.774	-1.389	2.153	1.243	-0.059	4
5.90	-1.462	-1.574	-0.793	1.784	4.895	1.487	1.953	2.877	-0.031	1.044	15
6.10	4.072	4.061	1.557	-0.345	-0.356	-3.801	-0.013	-4.869	-5.458	-5.185	4
6.50	0.320	-2.159	0.689	-0.731	0.544	-0.226	-0.375	0.524	-0.554	0.413	4
6.70	2.542	-0.193	-0.378	-1.175	-1.334	-1.365	2.048	-0.372	-0.829	-0.673	25
6.90	2.360	1.813	3.379	3.316	3.046	7.530	4.223	2.591	2.588	2.585	14
7.30	5.915	5.242	4.546	3.199	4.956	3.133	3.633	4.263	7.501	4.647	4

During data processing, indications of a trend in gravity change over time, as the time of the earthquake approached, were observed by visual inspection of the plots. Figure 2 presents indicative, randomly selected plots of gravity values and their time derivatives against earthquake magnitudes. Recall that magnitude (mag) measurements are all in the mww scale. To verify and accurately measure them, the slopes of the gravity values over time, as the time of the earthquake was approached, were calculated from the earthquake time-series data for each earthquake. Plots of earthquake magnitudes against their preseismic time-series gravity slopes and their time derivatives were constructed. In a pilot investigation step, earthquake magnitude prediction was also attempted by applying multiple linear regression on their magnitude derivatives.

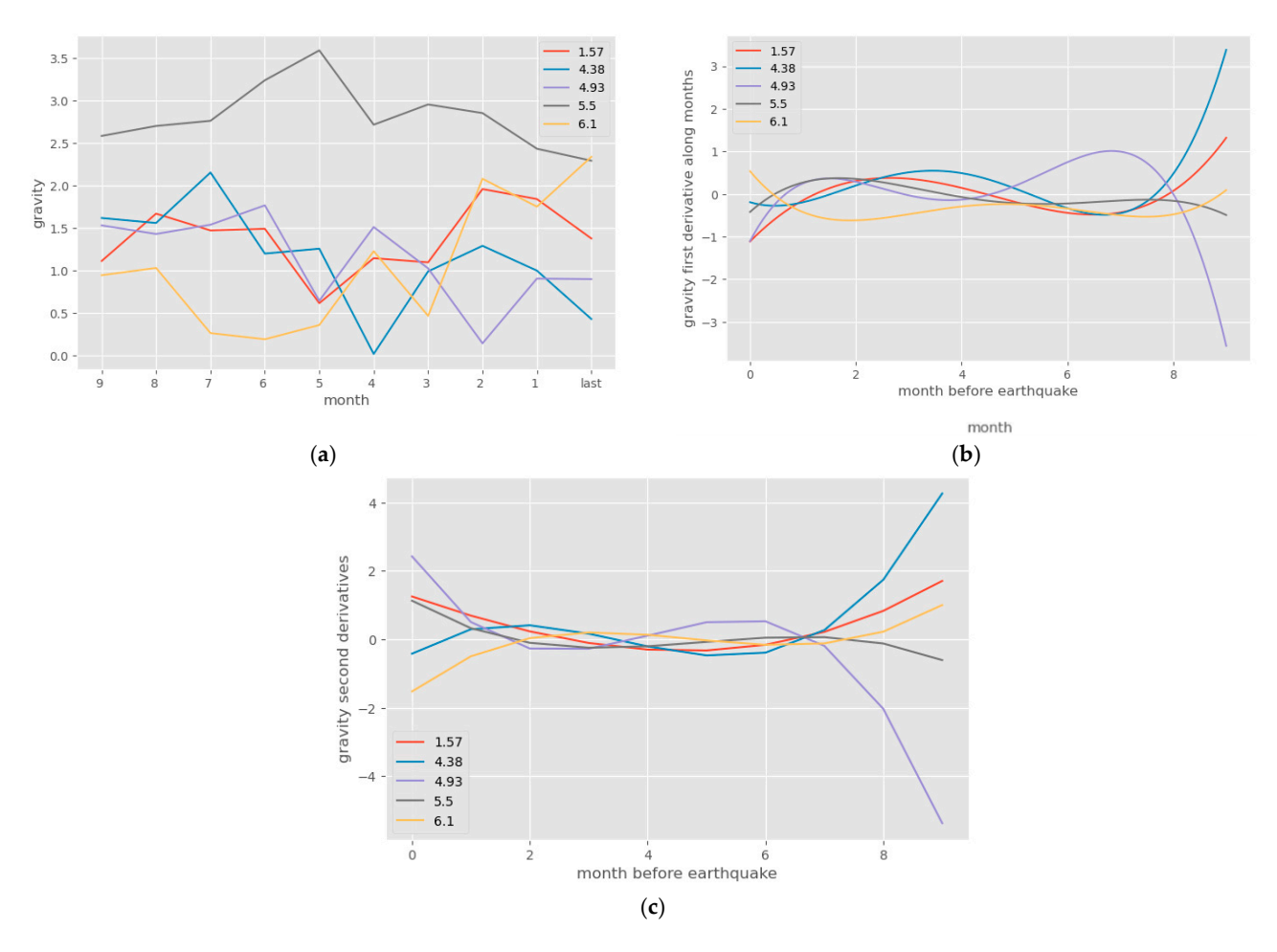


Figure 2. Plots of (a) gravities; (b) first derivatives; (c) second derivatives, against time before an earthquake. Randomly selected earthquakes are shown to avoid plot overcrowding. They are shown by their magnitude in the legend. Gravity values fluctuate unpredictably over time, in a way unrelated to the earthquake magnitude. The gravity rate of change (first derivative over time) and its acceleration (second derivative) also do not show any pattern associated with the earthquake magnitude.

Figure 3 shows the MLR results of attempts to predict earthquake magnitudes from the time series of gravity and its derivatives. It is clear from the results presented in Figure 3 that there is no connection between gravity time series and magnitudes; gravities over the epicenter fluctuate unpredictably over time. Wave-like patterns are observed for the first and second time derivatives, but with phases, wavelengths, or amplitudes unrelated to the earthquake magnitudes. In accordance with that, negative R² values were produced by the attempted prediction models, indicating no correlation between the gravities or their time derivatives to the earthquake magnitudes. Also, large mean-squared errors were produced.

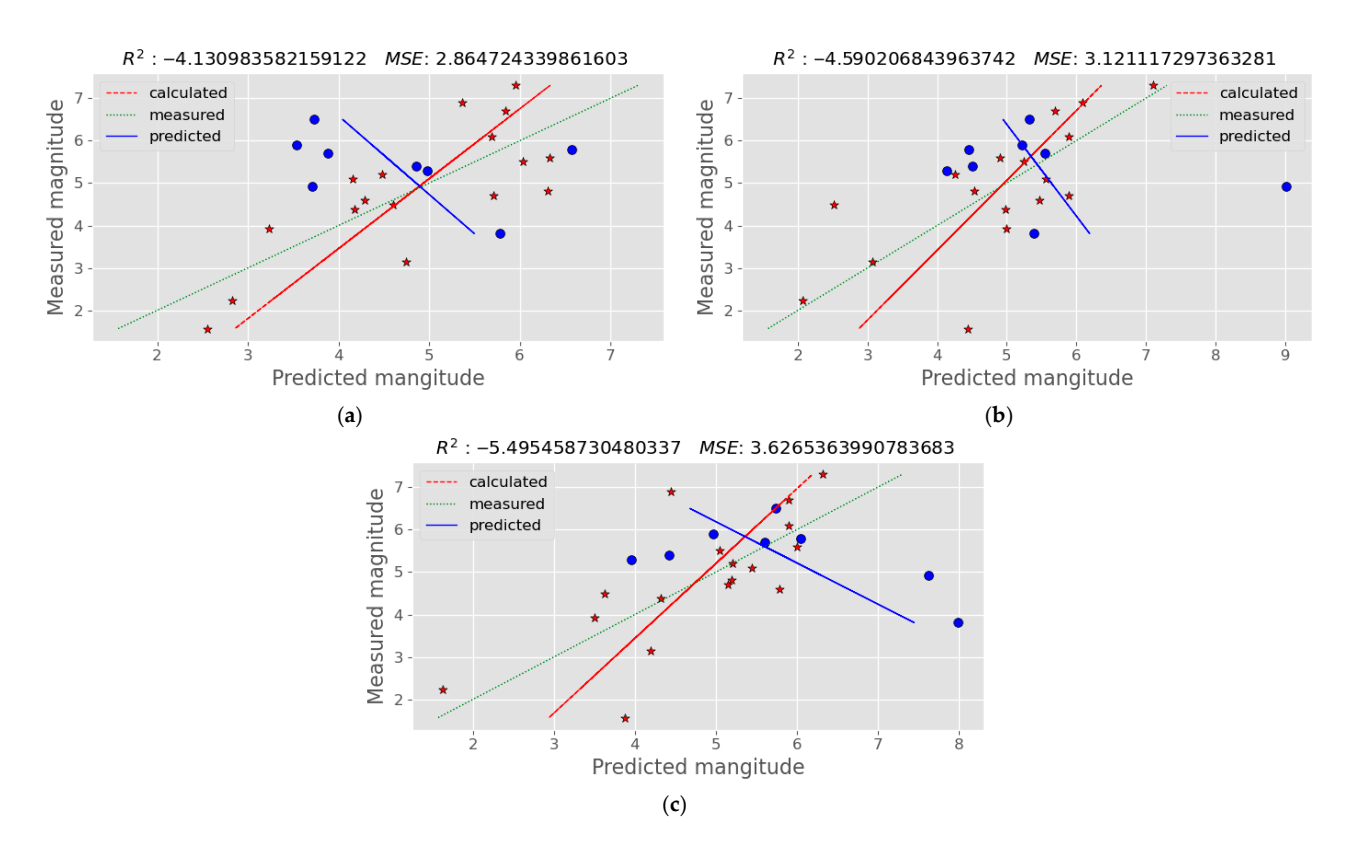


Figure 3. Plots of actual earthquake magnitudes against the values predicted by multiple linear regression using (a) the gravity values of the dataset; (b) their first-order time derivatives; (c) their second-order time derivatives. Neither the time series of gravity values over the earthquake epicenters, nor their time derivatives, are correlated to the earthquake magnitude. Blue dots indicate the generated values, while blue trend line indicates how well this predictions align with the actual measurements; red stars are the calculated data, while the red trend line shows the relationship between calculated and measured values. Green dotted trend line shows the internal consistency of measured data.

The first-order magnitude derivatives of gravity show the amount by which the gravity changes for an infinitesimally small, but always the same, change in earthquake magnitude. In Figure 4, it can be seen that this relates to the earthquake magnitude. Progressively larger gravity values are associated with larger magnitudes (Figure 4a), although a fluctuation is evident, curiously more intense in the range of 4.5 to 6.5. The first-order magnitude derivative plot (Figure 4b) reveals an interesting phenomenon. For small magnitudes, up to 4.5, the derivative is positive but with a negative slope. The second-order magnitude derivative for the same magnitude interval is negative with a positive slope (Figure 4c). A possible explanation and conclusion could be that as the lithosphere becomes denser and 'tighter', increasingly resisting large changes in its density, earthquakes that occur would be of a larger magnitude. In the interval of 5.8 to 7.3, the first derivative is again positive, but with a positive slope, while the second derivative is becoming increasingly positive (positive slope). Once again, larger earthquakes are associated with a denser lithosphere, but there is no resistance to further densening. The intriguing range is between 4.5 and 5.8, where a drop in the first and second derivative values is observed. Both the rate of gravity changes and the acceleration of this change decline to reach negative values. The lithosphere is at first still resistant to further densening. But as this resistance is weakening, as indicated by the negative derivatives, larger earthquakes occur. No increase in gravity is observed in this magnitude range, but an oscillatory fluctuation and a negative first derivative are. This indicates a negative 'speed' of gravity change. Decreases in gravity values occur for each unit of change in magnitude to achieve earthquakes of these magnitudes. The curves of

second-order derivatives are in agreement with those of the first derivatives. Notably, the curve patterns are similar for almost all months before the earthquake.

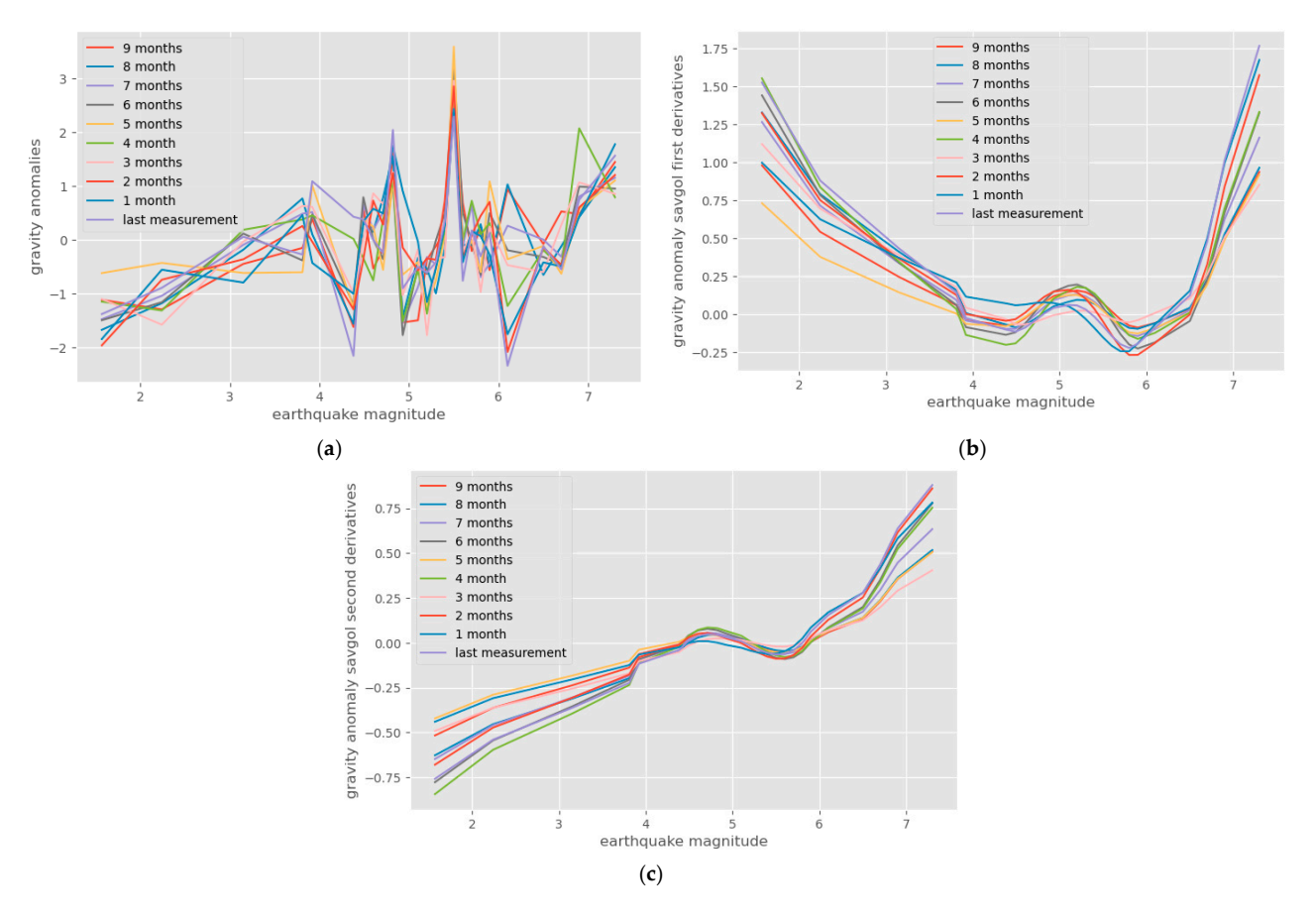


Figure 4. (a) Plots of gravity values; (b) their first-order magnitude derivatives; (c) second-order magnitude derivatives, against earthquake magnitudes and for various time periods in months before the earthquake occurrence, using the global dataset. Similar patterns were observed for all months. Gravity values are higher at all months for earthquakes of greater magnitudes, although they oscillate widely in the range of 4 to 6.5. The first derivatives are negative in magnitude in the range of 5.5 to 6.5 for most months. They gradually decrease to approach zero in the region of almost zero to four and increase precipitously for magnitudes above six. These alterations are correspondingly reflected in the shapes of the second-order derivatives.

Figure 5 illustrates the plots of actual earthquake magnitudes against the values predicted by MLR using the first-order and the second-order magnitude derivatives of the gravity values, whereas Figures 6 and 7 show the results of PLS regression and neural network, respectively. All three methods indicate a correlation of the earthquake magnitude to the first- and second-order magnitude derivatives, with MLR slightly better, followed by the neural network, but with the PLS regression not falling significantly behind in predictive efficiency. The first-order magnitude derivatives are a comparatively better predictor dataset than the second-order derivatives.

A summary of the prediction performance of the three machine learning algorithms on the gravity values and their derivatives is given in Table 3. The first- and second-order magnitude derivatives are very well correlated to the earthquake magnitudes with any of the three machine learning methods used. Good correlation was also observed when the third-order magnitude derivatives of the gravity time slopes were used. Large MSEs and negative \mathbb{R}^2 scores were obtained when the gravity values themselves or their time

derivatives were used. Negative R² values signify a correlation even worse than if the average values of the gravities or their derivatives were used.

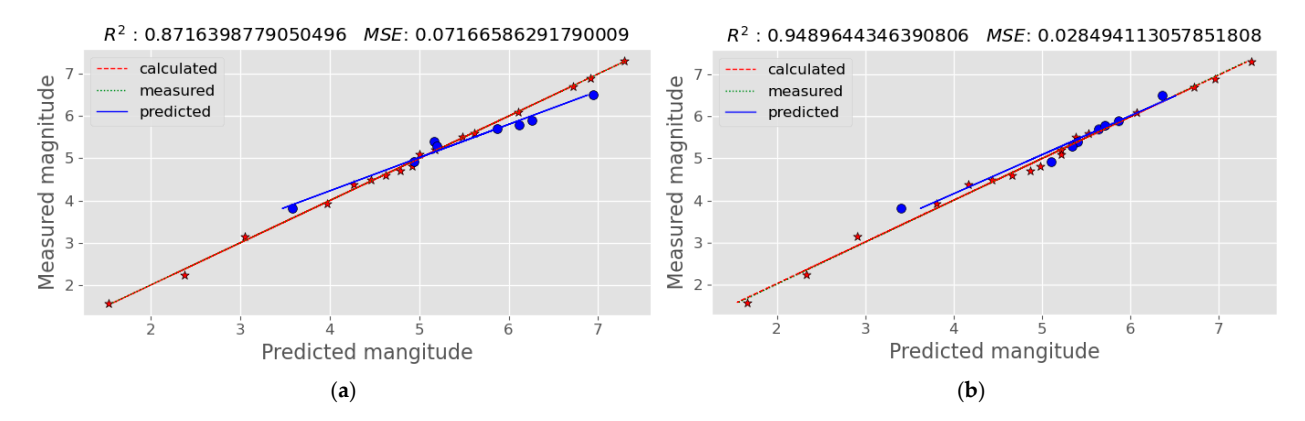


Figure 5. Plots of actual earthquake magnitudes against the values predicted by MLR using (a) the first-order magnitude derivative; (b) the second-order magnitude derivative of gravity values. The correlation between the earthquake magnitude and the rate of gravity change for each infinitely small change in the magnitude of the earthquake (first derivative-over-magnitudes) allows a very accurate prediction of the earthquake magnitude. Better predictions can be made using the second-order derivatives. Blue dots indicate the generated values, while blue trend line indicates how well this predictions align with the actual measurements; red stars are the calculated data, while the red trend line shows the relationship between calculated and measured values. Green dotted trend line shows the internal consistency of measured data.

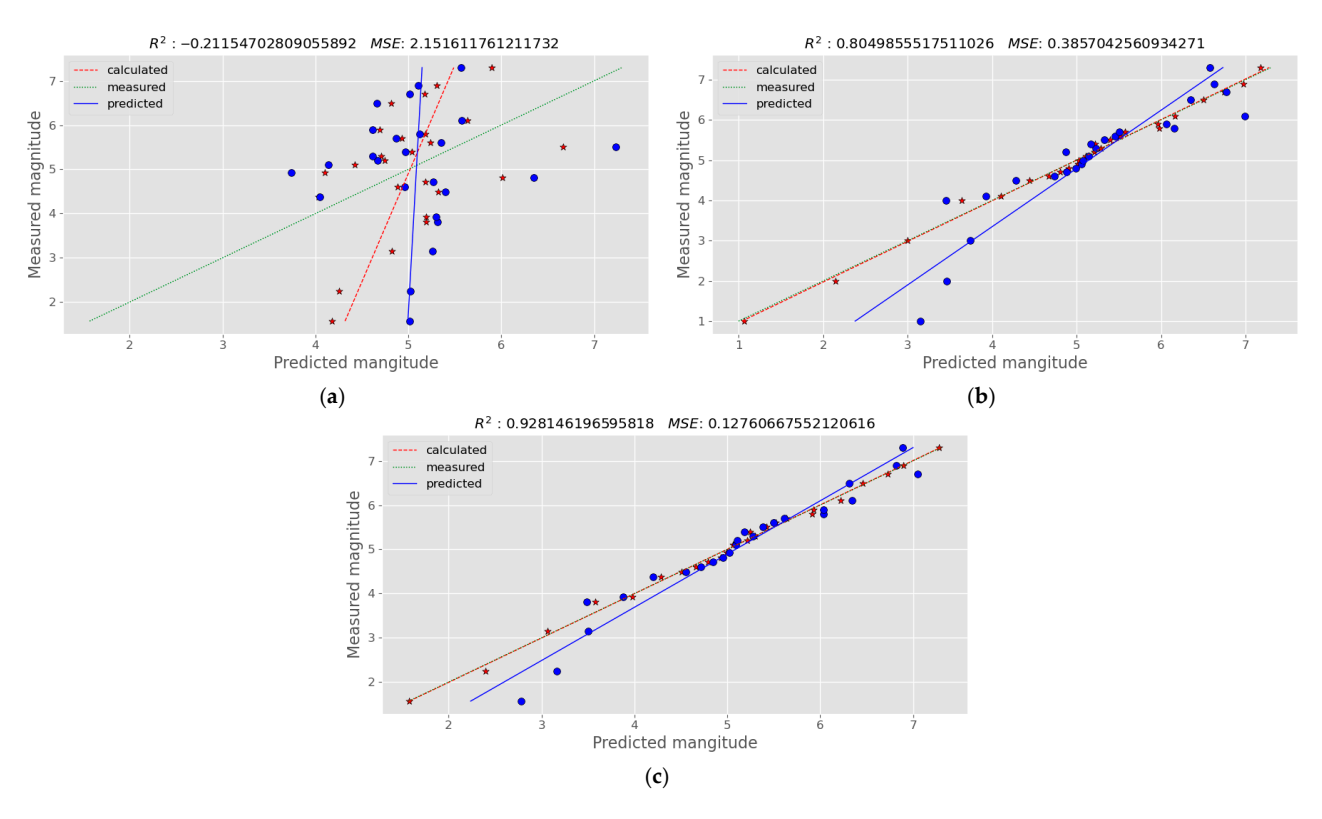


Figure 6. Plots of actual earthquake magnitudes against the values predicted by PLS using (\mathbf{a}) the gravity data; (\mathbf{b}) their first-order magnitude derivatives; (\mathbf{c}) their second-order magnitude derivatives. The best correlation of the earthquake magnitude, as inferred by the R^2 score, is with the first-order magnitude derivatives of the gravity values. Blue dots indicate the generated values, while blue trend line indicates how well this predictions align with the actual measurements; red stars are the calculated data, while the red trend line shows the relationship between calculated and measured values. Green dotted trend line shows the internal consistency of measured data.

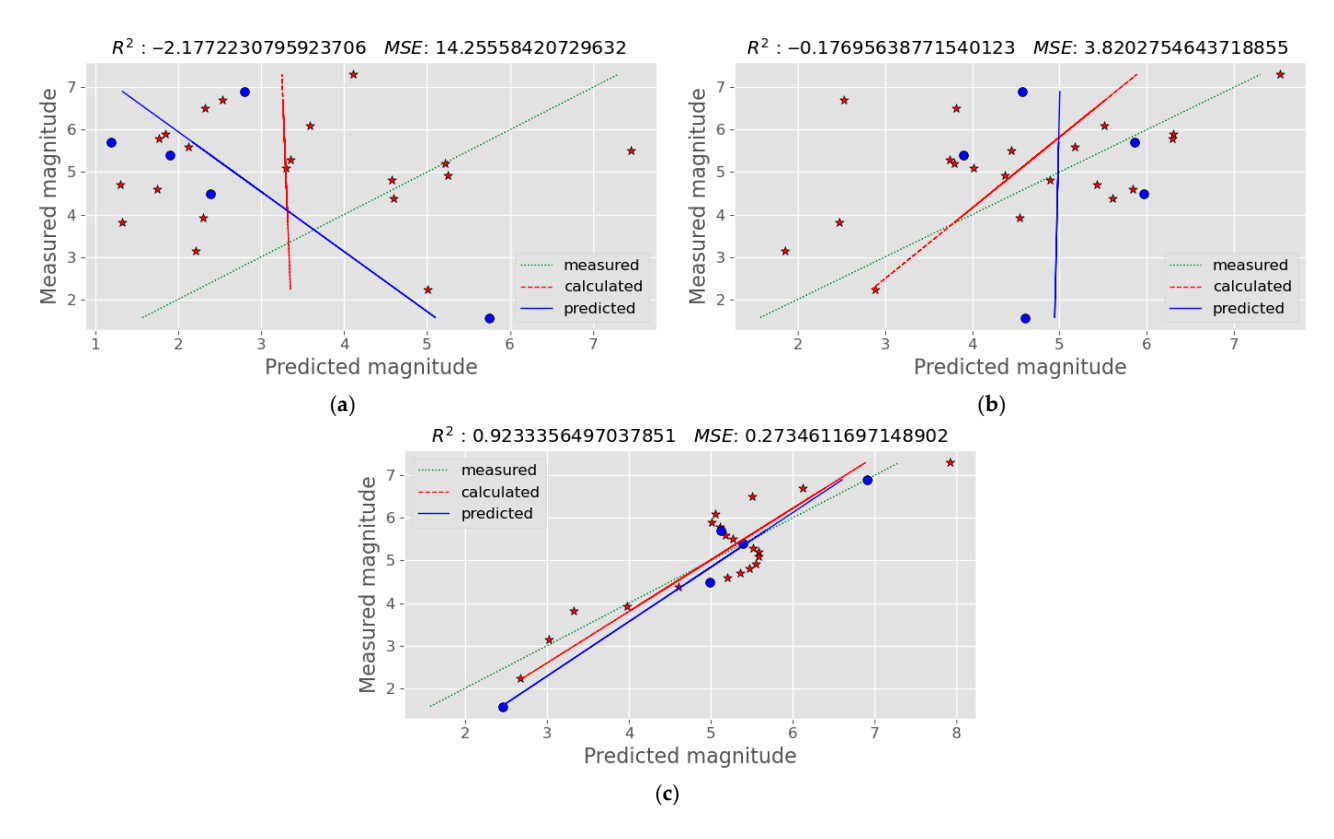


Figure 7. Plots of actual earthquake magnitudes against the values predicted by NN using (a) the gravity anomaly values; (b) the first-order magnitude derivative; (c) the second-order magnitude derivative of the gravity values. The best correlation of the earthquake magnitude, as inferred by the R^2 score and MSE value, is with the second-order magnitude derivatives of the gravity values. Blue dots indicate the generated values, while blue trend line indicates how well this predictions align with the actual measurements; red stars are the calculated data, while the red trend line shows the relationship between calculated and measured values. Green dotted trend line shows the internal consistency of measured data.

Table 3. MSE and R^2 (coefficient of determination) regression score for the correlation of earthquake magnitude from their gravity values and their derivatives over their epicenter, using various machine learning methods, on the global dataset.

	N	1LR	F	PLS .	N	IN
	MSE	R ² Score	MSE	R ² Score	MSE	R ² Score
Gravity values	2.864	-4.130	2.151	-0.211	11.860	-1.545
1st magnitude derivative	0.071	0.871	0.127	0.928	0.191	0.940
1st time derivative	3.121	-4.590	2.116	-0.192	4.291	-0.182
2nd magnitude derivative	0.028	0.948	0.131	0.926	0.273	0.923
2nd time derivative	3.626	-5.495	1.978	-0.114	7.553	-1.030
Slope 3rd magnitude derivative	2.864	-4.130	2.151	-0.211	11.860	-1.545

3.2. Results on the Greek Dataset

The characteristics of the Greek earthquake dataset are provided in Table A2 in the Appendix A section. Table 4 includes the gravity anomaly values at their epicenters as five measurements 10 days apart, while the last measurement is taken as close to the day of the earthquake as possible. Recall that magnitude (mag) measurements are all in the mww scale.

Table 4. The magnitude (mag) and gravity anomaly value over the earthquake epicenter on the first day closest to the day of the earthquake ('last measurement') and for each of the five 10-day intervals before that last measurement. The time lag between the day of the earthquake and the last measurement of gravity anomaly is given in the column 'days after last measurement' and depends on the available data in the COST-G Plotter gravity database.

Mag	Days After Last Measurement	Last Measurement	10 Days	20 Days	30 Days	40 Days	50 Days
2.71	7	-0.665	-0.386	-0.503	0.238	-0.438	0.052
2.91	6	0.817	1.031	0.517	0.728	-0.660	-1.309
2.98	2	-1.483	-0.964	-1.787	-0.573	-1.319	-2.641
3.05	5	0.439	-0.586	0.164	1.085	1.670	1.638
3.12	8	-0.022	3.567	0.120	2.772	5.024	0.111
3.37	15	2.155	4.949	3.695	2.672	3.271	2.827
3.81	5	-3.674	-2.813	-2.314	-3.629	-2.234	-2.255
3.92	3	0.962	0.408	2.035	0.966	1.041	0.533
4.03	2	1.892	2.155	2.863	3.689	4.217	3.337
4.30	2	1.552	2.646	2.042	1.738	2.334	3.304
4.38	9	1.248	1.552	1.050	1.180	1.161	1.099
4.49	9	-0.583	1.290	-2.100	-2.683	-2.627	-4.802
4.25	5	3.745	3.237	3.858	2.852	1.635	2.059
4.70	1	3.966	5.240	3.552	2.874	2.715	1.944
4.71	13	-0.280	-0.442	1.513	-1.728	-2.296	-2.171
4.90	8	4.907	0.536	4.569	4.866	3.655	1.786
5.00	2	4.779	3.889	3.028	4.914	3.689	4.271
5.10	7	0.748	-0.082	-0.064	0.200	0.148	-2.086
5.20	7	2.771	1.793	1.597	2.318	1.574	1.103
5.30	5	-3.235	-2.493	-2.009	-3.333	-1.940	-1.945
5.40	1	-0.950	0.526	0.808	0.394	1.118	0.587
5.50	3	-0.994	1.306	-2.422	0.198	0.441	0.643
5.60	7	1.457	-1.820	-2.383	-2.275	-4.461	-5.903
5.70	5	-0.248	-1.054	-1.715	0.706	-0.062	0.368
5.90	3	1.744	2.939	1.980	1.220	1.351	0.532
7.00	5	-3.205	-2.497	-2.036	-3.357	-1.949	-1.975

A correlation of the magnitudes of the earthquakes that occurred in Greece to the gravity anomaly values over their epicenters and the derivatives of these values was implemented. Figure 8 includes the plots of gravity values and their first-order derivatives, as well as the second-order magnitude derivatives, against earthquake magnitudes and for various time periods in days before the earthquake occurrence. Similar patterns are observed for all measurements. Derivative values are higher for earthquakes of greater magnitudes, although they oscillate in the range of 4 to 6.0. The shapes of the first- and second-order derivatives are similar to those of the corresponding plots for the set of global earthquakes for the same magnitude range, with negative derivatives in approximately the same magnitudes between 4.5 and 6.0. The first derivatives are negative in magnitude in the range between 4.8 and 5.8, while they increase rapidly for magnitudes above six. These alterations are correspondingly reflected in the shapes of the second-order derivatives, as observed from the figure.

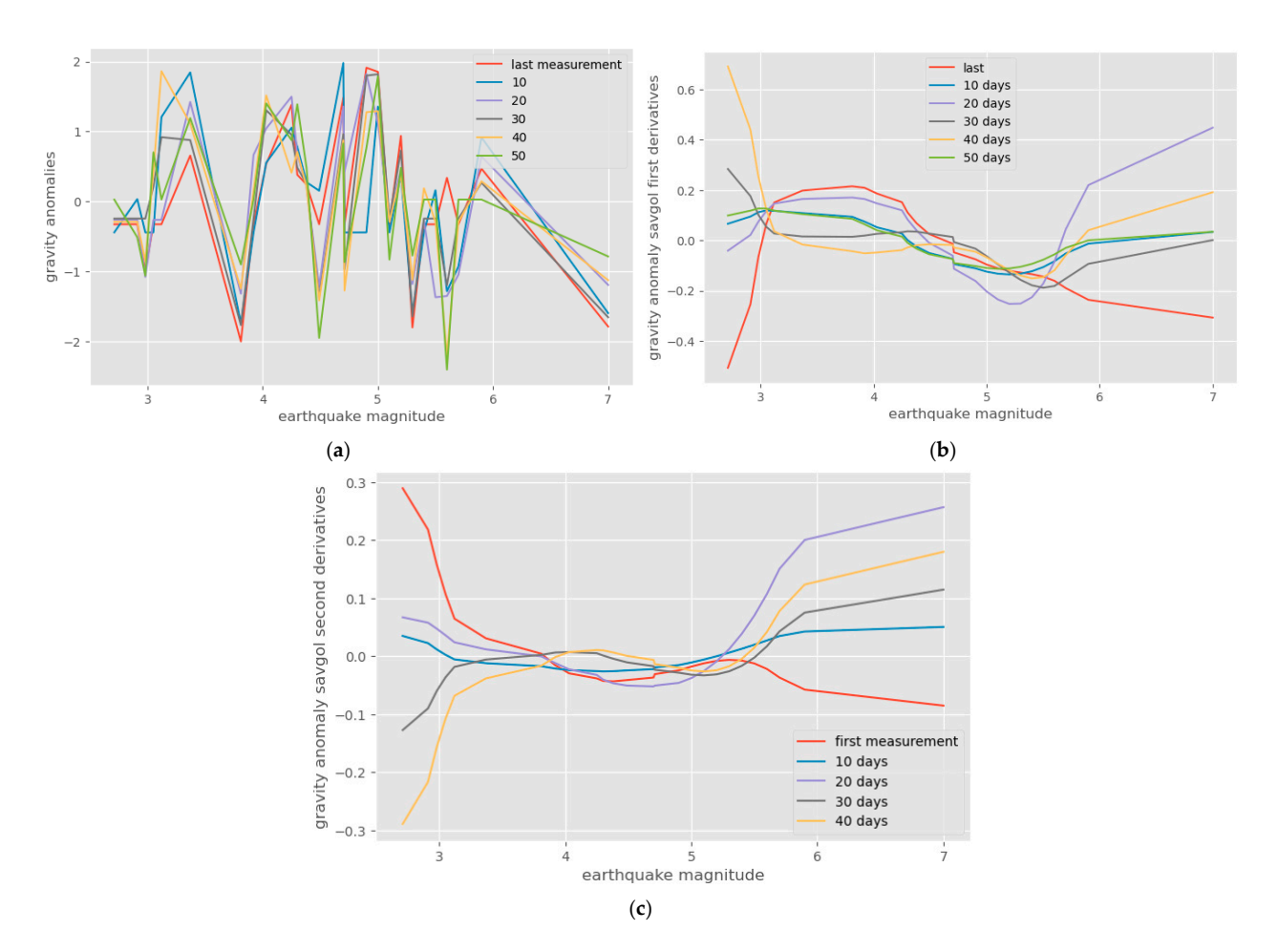


Figure 8. (a) Plots of gravity values; (b) their first-order derivatives; (c) second-order magnitude derivatives, against earthquake magnitudes and for various time periods in days before the earthquake occurrence, using the Greek dataset.

Figure 9 illustrates the results of MLR and PLS regression on the Greek dataset, by using the first-order and the second-order magnitude derivatives. Except for MLR using the first-order derivatives, the rest of the results exhibit excellent correlation between the magnitude derivatives and the earthquake magnitude. The best performance is achieved with MLR on the second-order derivatives, showing an MSE of 0.011 and a correlation score R² of 0.977. The combined results for all three machine learning methods are shown in Table 5. Once again, the magnitude derivatives are ones better associated with the earthquake magnitudes, while the raw gravity anomaly values and their time derivatives show no relation to the magnitudes.

Table 5. MSE and R^2 (coefficient of determination) regression score for the correlation of earthquake magnitude from their gravity values and their derivatives over their epicenter, using various machine learning methods, on the Greek dataset.

	N	ILR	F	PLS	1	NN
_	MSE	R ² Score	MSE	R ² Score	MSE	R ² Score
Gravity values	2.072	-0.923	1.303	-0.163	2.056	-0.986
1st magnitude derivative	0.066	0.932	0.500	0.553	0.436	-0.603
1st time-derivative	0.562	0.065	1.086	0.029	1.671	-0.449
2nd magnitude derivative	0.011	0.980	0.153	0.862	0.685	0.456
2nd time-derivative	1.886	-0.750	1.216	-0.086	2.199	-0.953

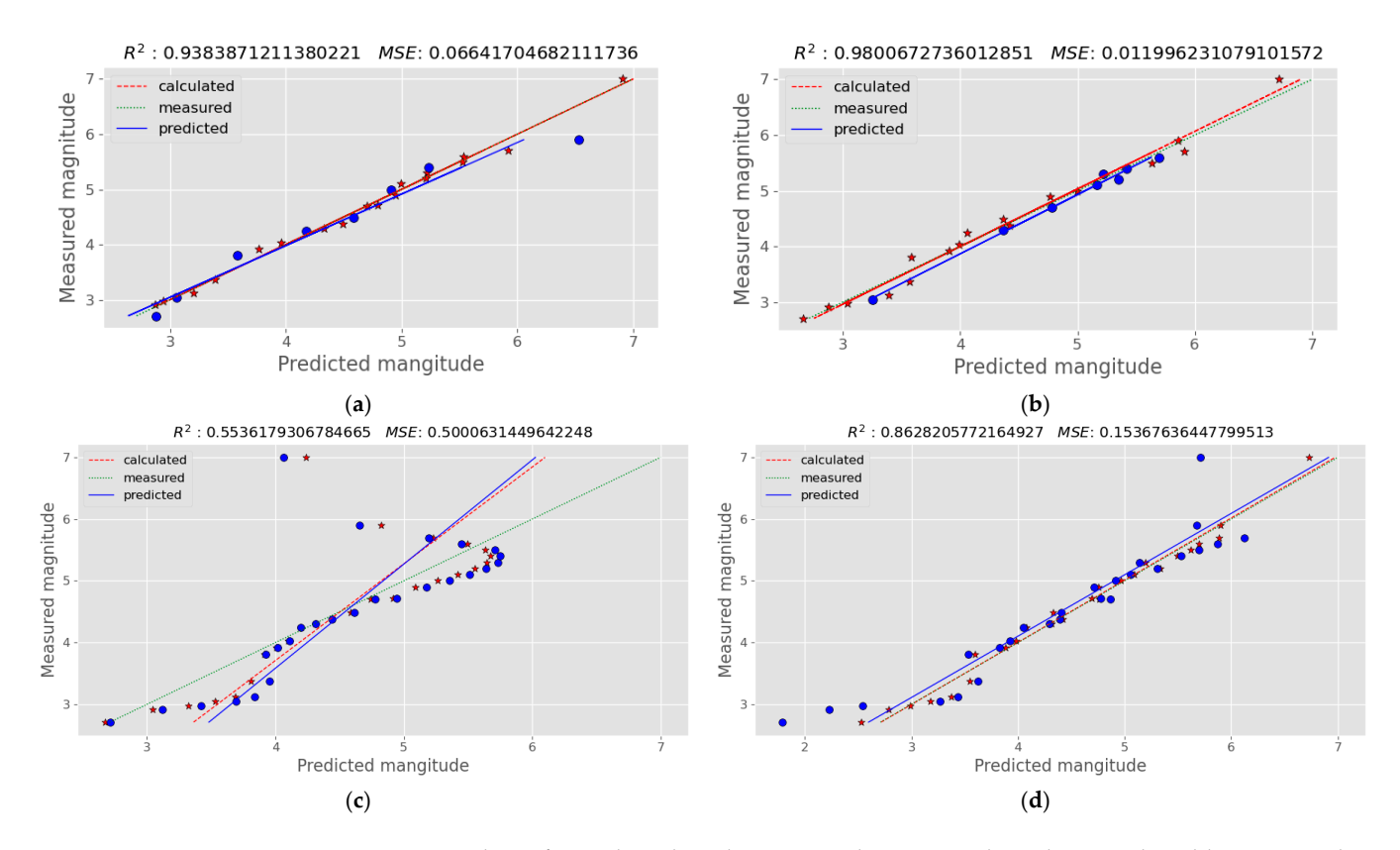


Figure 9. Plots of actual earthquake magnitudes against the values predicted by MLR and PLS regression for the Greek dataset: (a) MLR with the first-order magnitude derivatives; (b) MLR with the second-order magnitude derivatives; (c) PLS regression with the first-order magnitude derivatives; (d) PLS regression with the second-order magnitude derivatives. Blue dots indicate the generated values, while blue trend line indicates how well this predictions align with the actual measurements; red stars are the calculated data, while the red trend line shows the relationship between calculated and measured values. Green dotted trend line shows the internal consistency of measured data.

3.3. Results on the Hellenic Trench Dataset

The characteristics for the Hellenic Trench dataset are provided in Table A3 in the Appendix A section. The gravity anomaly values for the dataset of the earthquakes that occurred in the Hellenic Trench region are presented in Table 6. The dataset contains earthquakes of magnitude over 5.0 mww. In this case, no conversion of the magnitude scale was necessary. The first-order and the second-order magnitude derivative plots against the earthquake magnitudes are shown in Figure 10. In agreement with the first-order magnitude derivative shapes on the other two earthquake datasets (Figures 4 and 8), negative values are observed in the approximate region of 5.0 to 6.0 mww. The exact areas of negative values vary somewhat, since quite different datasets are used. Very good correlations of the earthquake magnitudes to the magnitude derivatives were obtained with both MLR and PLS regression, especially with the second-order derivatives. Figure 11 illustrates the results of MLR and PLS regression on the Hellenic Trench dataset, by using the first-order and the second-order magnitude derivatives. A summary of the results obtained by all three ML methods is given in Table 7. It should be noted that the results lead to the same assumptions as in all previous experimental cases.

Table 6. The magnitude (mag) and gravity anomaly value over the earthquake epicenter on the first day closest to the day of the earthquake ('last measurement') and for each of the five 10-day intervals before that last measurement, for the Hellenic trench dataset. The time lag between the day of the earthquake and the last measurement of gravity anomaly is given in the column 'days after last measurement' and depends on the available data in the COST-G Plotter gravity database.

Mag	Days After Last Measurement	Last Measurement	10 Days	20 Days	30 Days	40 Days	50 Days
5.00	3.6	0.636	-0.295	-0.323	0.191	0.403	-1.514
5.10	4.4	-1.615	-1.544	-0.118	0.604	-0.320	-0.301
5.20	3.6	0.688	-0.223	-0.260	0.202	0.341	-1.644
5.30	8.0	0.423	0.835	1.844	0.242	2.119	2.656
5.40	8.0	0.305	0.800	-0.043	-0.080	0.220	0.159
5.50	1.5	0.799	0.810	-0.223	0.127	-0.906	0.091
5.60	6.9	2.807	2.447	4.805	1.373	1.564	0.232
5.70	3.7	0.622	-0.308	-0.319	0.186	0.403	-1.524
5.90	3.3	1.744	2.939	1.980	1.221	1.352	0.533
6.00	6.9	3.786	2.515	3.083	3.846	3.931	3.982
6.40	2.6	0.996	2.296	0.914	0.485	1.366	0.274
6.50	7.3	-0.207	0.213	0.285	-1.760	-2.037	-2.490

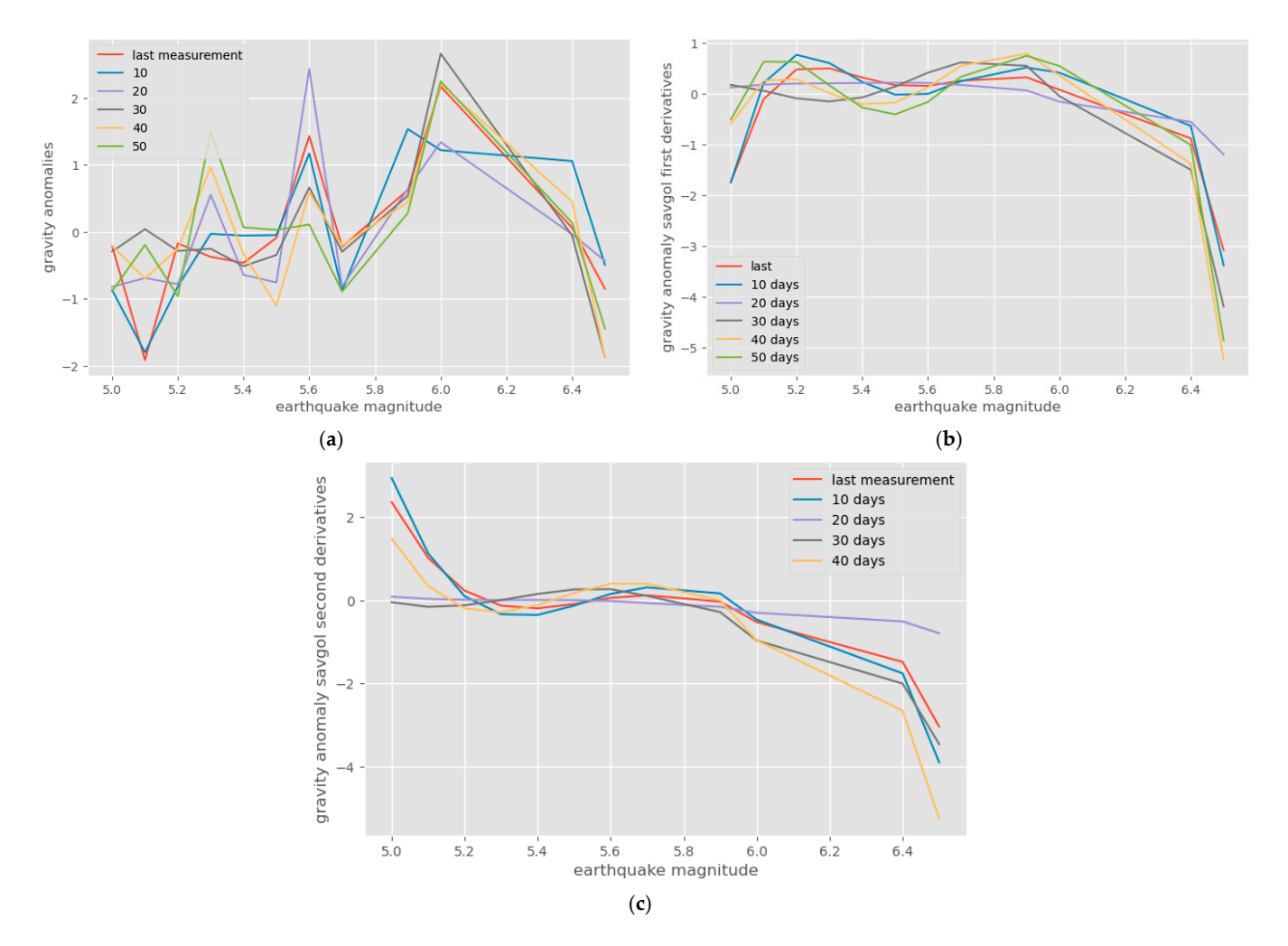


Figure 10. (a) Plots of gravity values; (b) their first-order magnitude derivatives; (c) second-order magnitude derivatives, against earthquake magnitudes and for various time periods in days before the earthquake occurrence, using the Hellenic Trench dataset.

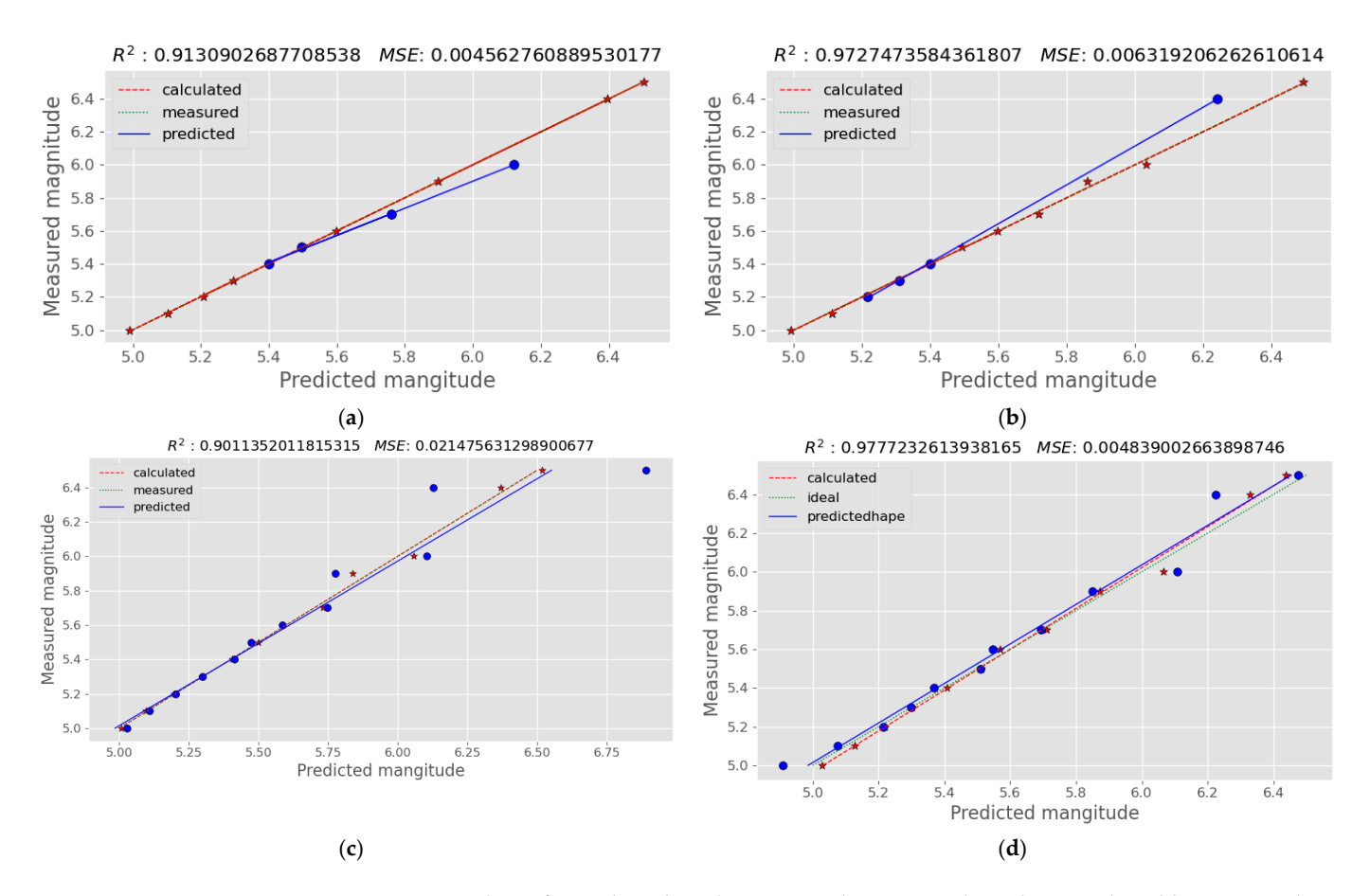


Figure 11. Plots of actual earthquake magnitudes against the values predicted by MLR and PLS regression for the Hellenic Trench Dataset: (a) MLR with the first-order magnitude derivatives; (b) MLR with the second-order magnitude derivatives; (c) PLS regression with the first-order magnitude derivatives; (d) PLS regression with the second-order magnitude derivatives. Blue dots indicate the generated values, while blue trend line indicates how well this predictions align with the actual measurements; red stars are the calculated data, while the red trend line shows the relationship between calculated and measured values. Green dotted trend line shows the internal consistency of measured data.

Table 7. MSE and R^2 (coefficient of determination) regression score for the correlation of earthquake magnitude to their gravity values and their derivatives over their epicenter, using various machine learning methods, on the Hellenic Trench dataset.

	N	ILR	F	PLS	N	JN
-	MSE	R ² Score	MSE	R ² Score	MSE	R ² Score
Gravity values	4.861	-91.600	0.238	-0.095	9.479	-100.03
1st magnitude derivative	0.004	0.913	0.021	0.901	1.064	-2.549
1st time-derivative	1.722	-6.428	0.283	-0.306	2.352	-32.933
2nd magnitude derivative	0.006	0.972	0.004	0.977	9.113	-48.970
2nd time-derivative	0.687	-12.103	0.269	-0.241	12.818	-40.710

4. Discussion

Despite the intense efforts by many researchers to predict earthquake occurrence and magnitude from gravity changes, the results are still far from satisfactory. This work shows that time series of gravity changes are not associated with earthquake magnitudes. Their first-order time derivatives represent the speed with which gravity changes take place,

and the second-order derivatives are the accelerations in the gravity changes. Gravity changes are supposed to be the result of lithospheric-level pressures and relaxations created by plate contacts or by convection currents of flowing masses under the plates. Since the gravity first-order time derivatives are not related to earthquake magnitude, it is not the speed of convectional mass flows, and in extension, their momentum, responsible for the magnitudes.

However, it is shown that the gravity magnitude derivatives are associated with earthquake magnitude. Since this first derivative is negative in the magnitude range between 4.5 and 6.5, we conclude that earthquakes of those magnitudes are associated with a looser crustal mass net and its lower density or with downwards positioning of magma masses. In contrast, larger magnitudes are associated with a denser crustal mass, perhaps the result of pressure between the plates or with magma masses positioned close to the surface. It must be emphasized that these are not time derivatives but magnitude derivatives. The meaning of this is that the changes in crustal density or magma positioning do not occur timewise before the earthquake but are already in place. Whatever the reason for triggering the earthquake, the magnitude is related to the already existing crustal density or magma positioning. The negative slopes of the first derivatives in the magnitude range of almost zero to 4 degrees indicate that looser masses or deeper magma positions help to cause earthquakes of gradually increasing magnitudes.

There is plenty of evidence that gravity alterations, caused by interaction with celestial bodies, such as the sun or moon, are contributing to earthquake occurrence [65–69]. In this work, we examined the gravity field vector perpendicular to the Earth's surface. Gravity field vectors exercised by celestial bodies horizontally to the Earth's surface are possible. Their pulling-pushing effect on lithospheric plates could be a cause of earthquakes. Due to the Earth's rotation, the perpendicular or horizontal effect of celestial gravity fields would last only a few hours, unlikely to be detected by the monthly or weekly recordings of the satellites. To our knowledge, no daily, let alone multiple daily, gravity recording exists yet.

It must be noted that the atmospheric pressure can affect the ground gravity [70–72]. The same applies to hydrology factors, including groundwater movements [73–77]. Regardless of the cause, it is ultimately changes in gravity that play a role in triggering earthquakes. Although the effect of groundwater could also be attributed to crust extension or contraction [78], no such explanation is possible for the atmospheric pressure. In conclusion, it is not only the underground pressures that stress the lithosphere, but the overground or surface forces also have a significant role in earthquakes' induction. In both cases, it is the crustal plates that receive both pressures, and this is recorded as changes in gravity.

A possible limitation of this work is the consideration of low-magnitude earthquakes in the methodology. Future work will consider extending the dataset by including high-magnitude earthquakes from Mw = 5.0 to Mw = 9.0. Yet, it should be noted that the latter is not always feasible, since most of the time, for most regions, there is a lack of actual acceleration time-history records, especially of high intensity, due to the absence of nearby seismic stations or due to low seismic variations.

This work does not intend to predict the occurrence or the magnitude of earthquakes; it aims to elucidate some of the relations of gravity to the magnitudes of the earthquakes. There are significant problems in attempting to predict earthquake magnitudes using derivatives. Since it is the magnitude derivatives that are related to earthquake magnitude, these derivatives must be calculated for any earthquake of unknown magnitude to be predicted. Yet, derivative calculations require the gravity values of the unknown-magnitude earthquake to be intercalated between the rows of a dataset of known-magnitude earthquakes. The exact intercalation position is not known since the new earthquake is of unknown magnitude. Also, the constructed MLR, PLS, or NN prediction model will be different after the intercalation of

the new earthquake. Preliminary prediction attempts were, however, made in this work; the results were not satisfactory, confirming our concerns, and therefore were not included.

5. Conclusions

This work aims to investigate the potential relationship between gravity field variations and earthquake magnitude using GRACE satellite data and advanced AI-based modeling techniques.

Three different earthquake datasets, one with large differences in the geodynamics of the epicenters and long time series of gravity data, one with more limited geodynamic differences and short time series data, and one with similar geodynamics, were used, resulting in the same shape of curves in the plots of magnitude derivative against earthquake magnitude. In both cases, there are negative first-order magnitude derivative values in approximately the same magnitude range between 4.5 and 6.0. While no direct correlation was found between gravity or its temporal derivatives and earthquake magnitude, strong predictive performance was achieved using magnitude derivatives. The derivatives of both datasets show very good correlation to the earthquake magnitudes, while the best results were obtained with MLR and poorer with the NN.

Our experimental findings indicate that, despite the fact that gravity changes do not determine the timing of seismic events, they are indicative of the underlying crustal density and magma dynamics that influence earthquake strength. Results emphasize that pre-existing geophysical conditions play a critical role in shaping the magnitude of an earthquake, offering valuable insight for future seismic risk assessment and modeling efforts.

Author Contributions: Conceptualization, E.V. and G.A.P.; methodology, C.C.; software, C.C.; validation, E.V., G.A.P. and C.C.; formal analysis, C.C.; investigation, C.C.; resources, C.C.; data curation, C.C.; writing—original draft preparation, C.C.; writing—review and editing, E.V. and G.A.P.; supervision, E.V. All authors have read and agreed to the published version of the manuscript.

Funding: This research received no external funding.

Institutional Review Board Statement: Not applicable.

Informed Consent Statement: Not applicable.

Data Availability Statement: The original data used in this work are included in Tables A1–A3.

Conflicts of Interest: The authors declare no conflicts of interest.

Abbreviations

The following abbreviations are used in this manuscript:

MLR multiple linear regression
PLS partial least squares
NN neural networks
ULF ultra-low frequency
VLF very low frequency
Ms surface wave magnitude
AI artificial intelligence

USGS United States Geological Survey Search Comprehensive Earthquake Catalogue

GRACE Gravity Recovery and Climate Experiment

IGFS International Gravity Field Service

COST-G Combination Service for Time-Variable Gravity

μGal microGalileo MSE) mean squared error

Appendix A

Table A1. The global dataset: dates, times, geographic coordinates of the epicenters, magnitude (mag.), depth, and location of the earthquakes used in this study. Magnitude scales: ml = local magnitude (Richter scale); md = duration magnitude scale; mb = body-wave magnitude (P-waves); mww = moment magnitude (from W-phase inversion).

Time	Latitude	Longitude	Mag	Depth	magType	dmin	rms	net	Id	Place	horizontalError	Depth Error	magError	Mag Nst	locationSource	magSource
2021-05-19 T10:41:12.805Z	38,182	-117,889	1	7.8	ml	0.025	0.08	nn	Nn 00807589	30 km SE of Mina, Nevada		0.5	0.24	8	nn	nn
2021-05-01 T02:14:48.715Z	32,116	-102,162	2	5.9	ml	0.015	0.1	tx	Tx 2021ilkv	15 km NNW of Midland, Texas	0.71	0.64	0.1	11	tx	tx
2021-05-13 T14:41:45.330Z	18,004	-66,760	3	11	md	0.158	0.15	pr	Pr 2021133006	1 km SE of Magas Arriba, Puerto Rico	0.33	0.24	0.16	10	pr	pr
2021-05-25 T04:24:46.561Z	24,755	122,495	4	10	mb	0.55	0.82	us	Us 6000efji	60 km WNW of Yonakuni, Japan	2.6	1.9	0.258	4	us	us
2021-05-27 T13:30:51.483Z	-27,092	-70,936	4.1	54.44	mb	0.581	1.39	us	Us 6000ef53	67 km WNW of Copiapo, Chile	5.7	10.7	0.302	3	us	us
2021-05-03 T15:19:57.804Z	53,802	160,385	4.5	71.99	mb	1298	0.58	us	Us 7000dzq0	142 km NE of Petropavlovsk- Kamchatsky, Russia	10.1	8.3	0.05	116	us	us
2021-05-03 T11:46:46.696Z	-61,875	-81 <i>,</i> 575	4.6	10	mb	3296	0.68	us	Us 7000dzp9	108 km SW of Sechura, Peru	8.2	1.9	0.073	56	us	us
2021-05-16 T17:32:48.435Z	27,745	52,142	4.7	10	mb	4588	0.75	us	Us 7000e3l3	76 km WNW of Mohr, Iran	8.6	1.5	0.057	94	us	us
2021-05-28 T13:06:35.311Z	24,877	122,549	4.7	10	mb	0.586	0.53	us	Us 6000egzm	64 km NW of Yonakuni, Japan	2.3	1.9	0.185	9	us	us
2021-05-21 T19:03:08.243Z	34,519	99,048	4.9	10	mb	4100	0.94	us	Us 7000e557	Southern Qinghai, China	7.8	1.8	0.057	98	us	us
2021-05-28 T07:24:16.071Z	36,524	70,135	5	209.8	mb	0.697	0.78	us	Us 6000efd7	25 km ESE of Farkhar, Afghanistan	5.9	5.5	0.053	112	us	us
2021-05-29 T01:25:14.219Z	1019	120,085	5.1	17.42	mww	0.702	0.88	us	Us 6000efq7	214 km N of Palu, Indonesia	4.8	3.3	0.086	13	us	us

Table A1. Cont.

Time	Latitude	Longitude	Mag	Depth	magType	dmin	rms	net	Id	Place	horizontalError	Depth Error	magError	Mag Nst	locationSource	magSource
2021-05-21 T23:56:16.899Z	5887	126,646	5.2	10	mb	5131	0.78	us	Us 7000e57i	73 km SE of Pondaguitan, Philippines	3.9	1.7	0.048	146	us	us
2021-05-05 T01:17:26.708Z	-20,697	-173,463	5.3	10	mww	6939	0.73	us	Us 7000e07n	134 km SE of Pangai, Tonga 74 km SE of	8.7	1.8	0.098	10	us	us
2021-05-21 T01:37:36.219Z	-9889	160,446	5.4	16.49	mww	0.664	1.04	us	Us 7000e4yd	Honiara, Solomon Islands	5.5	3.2	0.08	15	us	us
2021-05-29 T01:02:41.087Z	36,311	141,987	5.5	12.04	mww	3055	0.85	us	Us 6000efq6	122 km ENE of Hasaki, Japan	2.3	3	0.071	19	us	us
2021-05-03 T08:46:39.830Z	51,306	100,420	5.6	18	mww	2050	0.51	us	Us 7000dznc	28 km SW of Turt, Mongolia	7.3	1.8	0.065	23	us	us
2021-05-25 T21:36:44.310Z	-17,576	-174,808	5.7	201.18	mww	4551	0.83	us	Us 7000e68h	147 km NW of Neiafu, Tonga	10.9	3.7	0.051	37	us	us
2021-05-21 T12:09:22.756Z	-8421	112,332	5.8	106	mww	1801	0.65	us	Us 7000e50p	33 km SSW of Sumberpu- cung, Indonesia	3.6	1.9	0.062	25	us	us
2021-05-30 T20:47:51.021Z	-56,826	-140,710	5.9	10	mww	27476	0.75	us	Us 6000egs4	Pacific- Antarctic Ridge	15.2	1.8	0.086	13	us	us
2021-05-21 T13:48:37.193Z	25,727	100,008	6.1	9	mww	4438	0.93	us	Us 7000e532	25 km NW of Dali, China 265 km SSE	6.8	1.7	0.053	34	us	us
2021-05-21 T22:13:18.379Z	-16,601	-177,373	6.5	10	mww	4518	0.96	us	Us 7000e579	of Alo, Wallis and Futuna	7.3	1.4	0.061	26	us	us
2021-05-12 T14:05:15.667Z	-17,387	66,314	6.7	10	mww	10669	0.68	us	Us 7000e2ec	Mauritius- Reunion region	8.2	1.7	0.036	75	us	us
2021-05-01 T01:27:27.215Z	38,200	141,597	6.9	43	mww	2619	0.82	us	Us 7000dz5t	30 km SSE of Onagawa Cho, Japan	7.3	1.9	0.041	58	us	us
2021-05-21 T18:04:13.565Z	34,598	98,251	7.3	10	mww	4655	0.77	us	Us 7000e54r	Southern Qinghai, China	3	1.7	0.037	71	us	us

Table A2. The Greek dataset: dates, times, geographic coordinates of the epicenters, magnitude (mag), depth, and locality of the earthquakes that occurred in Greece and its neighborhood during the year 2020. Magnitude scales: ml = local magnitude (Richter scale); md = duration magnitude scale; mb = body-wave magnitude (P-waves); mww = moment magnitude (from W-phase inversion).

Time	Latitude	Longitude	Mag	Depth	magType	dmin	rms	net	Id	Place	horizontalError	Depth Error	magError	Mag Nst	locationSource	magSource
2020-07-22 T16:28:51.512Z	39,669	19,763	2.7	10	ml	0.049	0.84	us	us6000b2a3	8 km WNW of Kontokali	6.6	2.0	0.097	14	us	us
2020-05-11 T09:33:07.394Z	37,824	27,144	3.0	10	ml	1.297	0.67	us	us70009dzb	10 km WSW of Kusadasi	5.3	2.0	0.085	18	us	us
2020-04-27 T20:15:03.107Z	41,425	19,527	3.1	10	ml	1.023	0.62	us	us60009dg4	9 km NNW of Shijak	5.4	2.0	0.064	32	us	us
2020-06-01 T23:15:01.842Z	40,459	21,483	3.2	10	ml	0.847	0.26	us	us6000a401	7 km WSW of Emporio	3.9	2.0	0.077	22	us	us
2020-04-13 T23:56:37.740Z	41,603	28,747	3.3	10	ml	2.069	1.03	us	us70008vrx	33 km N of Durusu	4.6	2.0	0.085	18	us	us
2020-02-20 T00:32:32.386Z	35,272	23,962	3.6	10	mb	0.758	0.82	us	us70007tbw	17 km WNW of Chora Sfakion	3.4	2.0	0.352	2	us	us
2020-10-30 T12:41:31.954Z	37,797	26,977	4.0	10	mb	1.425	0.63	us	us7000cask	4 km N of Samos	5.8	1.9	0.195	7	us	us
2020-04-18 T23:36:53.658Z	38,073	20,321	4.1	21.78	mb	1.555	1.05	us	us70008zl8	17 km SW of Lixouri	5.0	6.2	0.100	27	us	us
2020-10-17 T20:31:59.067Z	39,108	23,415	4.2	10	mb	1.224	0.7	us	us6000c91f	8 km SW of Skiathos	4.9	1.9	0.264	4	us	us
2020-07-07 T15:19:51.452Z 2020-06-04	38,836	25,331	4.3	8.92	mb	2.118	0.74	us	us7000ajhc	38 km NNW of Psara 14 km SSW of	4.5	5.9	0.126	18	us	us
T04:51:18.397Z 2020-02-04	35,089	26,052	4.4	10	mb	0.972	0.75	us	us6000a9vs	Sitia 12 km NE of	6.1	1.9	0.178	9	us	us
T16:47:10.864Z 2020-10-30	38,997	27,941	4.5	10	mb	0.698	1.04	us	us60007phg	Akhisar 89 km S of	4.7	1.9	0.105	27	us	us
T09:20:36.917Z 2020-02-06	34,401	26,428	4.6	10	mb	1.291	0.58	us	us7000catf	Palekastro 10 km SSE of	5.1	1.9	0.164	11	us	us
T09:24:16.857Z 2020-02-18	39,254	21,497	4.7	10	mwr	1.393	0.9	us	us70007jsv	Anthiro 12 km E of	2.9	1.7	0.068	21	us	us
T16:09:23.758Z 2020-12-29	39,107	27,817	4.8	10	mb	0.534	0.68	us	us70007sgb	Kirkagac 14 km S of	2.8	1.8	0.060	87	us	us
T08:06:09.922Z 2020-08-17	34,709	24,069	4.9	10	mb	0.887	1.12	us	us6000d3y3	Kastri 56 km SSE of	5.0	1.4	0.052	149	us	us
T07:27:02.373Z 2020-05-22	36,897	23,770	5.0	95.34	mww	1.502	0.61	us	us6000bfuq	Hydra 60 km SSE of	5.4	1.5	0.056	31	us	us
T03:40:30.610Z 2020-10-12	34,483	25,886	5.1	10	mww	1.147	0.97	us	us70009n06	Ierapetra 49 km N of	6.0	1.8	0.056	31	us	us
T04:11:27.566Z 2020-10-30	35,644	26,246	5.2	10	mww	0.751	1.06	us	us6000c7nd	Palekastro 8 km NW of	3.3	1.7	0.050	38	us	us
T15:14:55.887Z 2020-09-26	37,831	26,822	5.3	10	mww	1.518	1.28	us	us7000c7zh	Kokkari 31 km SSE of	5.2	1.9	0.098	10	us	us
T22:50:25.082Z 2020-01-28	39,984	24,334	5.4	10.38	mww	1.585	0.58	us	us6000c1rq	Karyes 69 km ESE of	5.8	3.8	0.046	45	us	us
T15:38:34.436Z	35,218	27,891	5.5	10	mww	0.681	0.65	us	us60007i7j	Karpathos	5.2	1.7	0.052	35	us	us

Table A2. Cont.

Time	Latitude	Longitude	Mag	Depth	magType	dmin	rms	net	Id	Place	horizontalError	Depth Error	magError	Mag Nst	locationSource	magSource
2020-01-22 T19:22:16.298Z	39,072	27,838	5.6	5.6	mww	0.567	0.66	us	us60007d2r	15 km ESE of Kirkagac	4.1	3.1	0.057	30	us	us
2020-05-20 T23:43:16.920Z	35,159	20,277	5.7	13.45	mww	2.416	0.52	us	us70009m4x	224 km ŠW of Methoni	6.7	3.4	0.048	42	us	us
2020-09-18 T16:28:17.575Z	35,036	25,303	5.9	44	mww	0.421	0.78	us	us7000bpvt	12 km SSE of Arkalochori	5.9	1.9	0.050	39	us	us
2020-10-30 T11:51:27.348Z	37,897	26,783	7.0	21	mww	1.518	0.59	us	us7000c7y0	13 km NNE of Neon Karlovasi	1.4	1.8	0.036	75	us	us

Table A3. The Hellenic Trench dataset: dates, times, geographic coordinates of the epicenters, magnitude (mag), depth, and locality of the earthquakes that occurred in Greece and its neighborhood during the year 2020. Magnitude scales: ml = local magnitude (Richter scale); md = duration magnitude scale; mb = body-wave magnitude (P-waves); mww = moment magnitude (from W-phase inversion).

Time	Latitude	Longitude	Mag	Depth	magType	dmin	rms	net	Id	Place	horizontalError	Depth Error	magError	Mag Nst	locationSource	magSource
2020-05-18 T11:48:07.371Z	34.1328	25.5231	5.0	10	mww	1.265	0.71	us	us70009jm3	Greece	7.1	1.8	0.075	17	us	us
2020-06-19 T07:43:21.049Z	34.2871	25.5222	5.1	10	mww	1.126	0.62	us	us6000aepr	81 km S of NΓ©a AnatolΓ, Greece	7.1	1.9	0.08	15	us	us
2020-05-18 T04:18:17.970Z	34.1648	25.6205	5.2	10	mww	1.271	0.86	us	us70009jdm	93 km S of NΓ©a AnatolΓ, Greece	6.9	1.8	0.05	39	us	us
2021-09-28 T04:48:08.650Z	35.0817	25.2018	5.3	10	mww	0.328	0.94	us	us7000ff36	9 km SW of ArkalochΓ ³ ri, Greece	4.5	1.7	0.046	45	us	us
2020-06-03 T09:03:29.381Z	34.3323	25.8927	5.4	10	mww	1.26	0.62	us	us6000a52k	76 km S of IerΓ' petra, Greece	7.2	1.8	0.098	10	us	us
2020-01-30 T01:28:05.202Z	35.1565	27.8845	5.5	10	mww	0.708	0.9	us	us60007jpa	72 km ESE of Karpathos, Greece	5.3	1.8	0.055	32	us	us
2021-12-26 T18:59:02.711Z	35.1923	26.9659	5.6	10	mww	0.388	1.09	us	us6000gfhq	25 km S of Fry, Greece	5.7	1.8	0.056	31	us	us
2020-05-18 T23:22:35.162Z	34.1855	25.5173	5.7	10	mww	1.215	0.6	us	us70009k7k	Greece	5.5	1.7	0.073	18	us	us
2020-09-18 T16:28:17.575Z	35.0368	25.3034	5.9	44	mww	0.421	0.78	us	us7000bpvt	12 km SSE of ArkalochΓ ³ ri, Greece	5.9	1.9	0.05	39	us	us
2019-11-27 T07:23:42.383Z	35.7174	23.2284	6.0	69	mww	1.421	1.02	us	us70006dlt	45 km WNW of KΓssamos, Greece	6.5	1.9	0.051	37	us	us
2021-10-12 T09:24:05.099Z	35.1691	26.2152	6.4	20	mww	0.86	0.46	us	us6000ftxu	4 km SW of Palekastro, Greece	6.1	1.8	0.048	42	us	us
2020-05-02 T12:51:05.561Z	34.1818	25.7101	6.5	10	mww	1.293	1.01	us	us700098qd	91 km S of	6.7	1.8	0.048	42	us	us

References

1. Sadhukhan, B.; Chakraborty, S.; Mukherjee, S. Predicting the Magnitude of an Impending Earthquake Using Deep Learning Techniques. *Earth Sci. Inform.* **2023**, *16*, 803–823. [CrossRef]

- 2. Yegulalp, T.M.; Kuo, J.T. Statistical Prediction of the Occurrence of Maximum Magnitude Earthquakes. *Bull. Seismol. Soc. Am.* **1974**, *64*, 393–414. [CrossRef]
- 3. Akhoondzadeh, M. Earthquake Prediction Using Satellite Data: Advances and Ahead Challenges. *Adv. Space Res.* **2024**, 74, 3539–3555. [CrossRef]
- 4. Huang, F.; Li, M.; Ma, Y.; Han, Y.; Tian, L.; Yan, W.; Li, X. Studies on Earthquake Precursors in China: A Review for Recent 50 Years. *Geodyn.* **2017**, *8*, 1–12. [CrossRef]
- 5. Zhao, X.; Pan, S.; Sun, Z.; Guo, H.; Zhang, L.; Feng, K. State-of-the-Art Review Advances of Satellite Remote Sensing Technology in Earthquake Prediction. *Nat. Hazards Rev.* **2020**, 22, 03120001. [CrossRef]
- 6. Biswas, S. Exploring the Difficulties in Forecasting Earthquake Location with Inhomogeneous Ionospheric Perturbations. *Nat. Hazards* **2024**, *120*, 14727–14754. [CrossRef]
- 7. Hayakawa, M.; Schekotov, A.; Yamaguchi, H.; Hobara, Y. Observation of Ultra-Low-Frequency Wave Effects in Possible Association with the Fukushima Earthquake on 21 November 2016, and Lithosphere–Atmosphere–Ionosphere Coupling. *Atmosphere* 2023, 14, 1255. [CrossRef]
- 8. Kumar, S.; Kumar, S.; Kumar, A. Earthquakes Associated Subionospheric VLF Anomalies Recorded at Two Low Latitude Stations in the South Pacific Region. *J. Atmos. Sol. Terr. Phys.* **2022**, 229, 105834. [CrossRef]
- Surkov, V.V. An Overview of Theoretical Studies of Non-Seismic Phenomena Accompanying Earthquakes. Surv. Geophys. 2025, 46, 7–70. [CrossRef]
- 10. Panet, I.; Narteau, C.; Lemoine, J.; Bonvalot, S.; Remy, D. Detecting Preseismic Signals in GRACE Gravity Solutions: Application to the 2011 Tohoku M w 9.0 Earthquake. *J. Geophys. Res. Solid Earth* **2022**, 127, e2022JB024542. [CrossRef]
- 11. Tang, H.; Sun, W. Theories and Applications of Earthquake-Induced Gravity Variation: Advances and Perspectives. *Earthq. Sci.* **2023**, *36*, 376–415. [CrossRef]
- 12. Wang, H.; Song, D.; Shan, X.; Bin Wang, A. A Method for Extracting the Pre-Seismic Gravity Anomalies over the Tibetan Plateau Based on the Maximum Shear Strain Using GRACE Data. *Earth Planet. Phys.* **2024**, *8*, 589–608. [CrossRef]
- 13. Yang, J.; Chen, S.; Zhang, B.; Zhuang, J.; Wang, L.; Lu, H. Gravity Observations and Apparent Density Changes before the 2017 Jiuzhaigou Ms7.0 Earthquake and Their Precursory Significance. *Entropy* **2021**, *23*, 1687. [CrossRef] [PubMed]
- 14. Fedotov, S.A.; Maguskin, M.A.; Kirienko, A.P.; Zharinov, N.A. Vertical Ground Movements on the Coast of the Kamchatka Gulf: Their Specific Features in the Epicentral Zone of the August 17, 1983, Earthquake M = 6.9, before and After. *Tectonophysics* **1992**, 202, 157–162. [CrossRef]
- 15. Fujii, Y.; Nakane, K. Case 24 Reevaluation of Anomalous Vertical Crustal Movement Associated with the 1964 Niigata, Japan, Earthquake. *Pure Appl. Geophys.* **1997**, *149*, 115–127. [CrossRef]
- 16. Kaftan, V.I. An Analysis of Ground Movements and Deformations from 13-Year GPS Observations before and during the July 2019 Ridgecrest, USA Earthquakes. *J. Volcanol. Seismol.* **2021**, *15*, 97–106. [CrossRef]
- 17. Shifflett, H.; Witbaard, R. Multiple Precursors to the Landers Earthquake. Bull. Seismol. Soc. Am. 1996, 86, 113–121. [CrossRef]
- 18. Kopylova, G.N.; Boldina, S.V.; Serafimova, Y.K. Earthquake Precursors in the Ionic and Gas Composition of Groundwater: A Review of World Data. *Geochem. Int.* **2022**, *60*, 928–946. [CrossRef]
- 19. Nakamura, Y.; Wakita, H. Precise Temperature Measurement of Groundwater for Earthquake-Prediction Study. *Pure Appl. Geophys.* **1984**, 122, 164–174. [CrossRef]
- 20. Orihara, Y.; Kamogawa, M.; Nagao, T. Preseismic Changes of the Level and Temperature of Confined Groundwater Related to the 2011 Tohoku Earthquake. *Sci. Rep.* **2014**, *4*, 6907. [CrossRef]
- 21. Zhang, W.; Li, M.; Yang, Y.; Rui, X.; Lu, M.; Lan, S. Implications of Groundwater Level Changes before near Field Earthquakes and Its Influencing Factors—Several Earthquakes in the Vicinity of the Longmenshan-Anninghe Fault as an Example. *Front. Earth Sci.* 2025, *13*, 1541346. [CrossRef]
- 22. Akhoondzadeh, M.; Marchetti, D. Study of the Preparation Phase of Turkey's Powerful Earthquake (6 February 2023) by a Geophysical Multi-Parametric Fuzzy Inference System. *Remote Sens.* 2023, 15, 2224. [CrossRef]
- 23. Ganguly, N.D. Variation in Atmospheric Ozone Concentration Following Strong Earthquakes. *Int. J. Remote Sens.* **2009**, *30*, 349–356. [CrossRef]
- 24. Nikolopoulos, D.; Cantzos, D.; Alam, A.; Dimopoulos, S.; Petraki, E. Electromagnetic and Radon Earthquake Precursors. *Geosciences* **2024**, *14*, 271. [CrossRef]
- 25. Gupta, H.K.; Singh, H.N. Earthquake Swarms Precursory to Moderate to Great Earthquakes in the Northeast India Region. *Tectonophysics* **1989**, *167*, 285–298. [CrossRef]
- 26. Kayal, J.R. Earthquake Prediction in Northeast India—A Review. Pure Appl. Geophys. 1991, 136, 297–313. [CrossRef]

Appl. Sci. 2025, 15, 11126 25 of 26

27. Bouih, M.; Panet, I.; Remy, D.; Longuevergne, L.; Bonvalot, S. Deep Mass Redistribution Prior to the 2010 Mw 8.8 Maule (Chile) Earthquake Revealed by GRACE Satellite Gravity. *Earth Planet. Sci. Lett.* **2022**, *584*, 117465. [CrossRef]

- 28. Gunawan, I.; Wahyudi, E.J.; Alawiyah, S.; Kadir, W.G.A. Earthquake Events Detected by Continuous Gravimeters in Indonesia. *J. Phys. Conf. Ser.* **2024**, 2734, 012006. [CrossRef]
- 29. Kazama, T.; Okubo, S.; Sugano, T.; Matsumoto, S.; Sun, W.; Tanaka, Y.; Koyama, E. Absolute Gravity Change Associated with Magma Mass Movement in the Conduit of Asama Volcano (Central Japan), Revealed by Physical Modeling of Hydrological Gravity Disturbances. *J. Geophys. Res. Solid. Earth* 2015, 120, 1263–1287. [CrossRef]
- 30. Liang, X.; Chen, S.; Chu, F.; Xu, R.; Sun, H.; Xiao, W.; Song, H.; Li, S. Resolution Analysis of the Gravity Survey Network in the Middle and South Sections of Tan-Lu Fault and Recent Changes in the Gravity Field. *Geod. Geodyn.* 2025, 16, 241–250. [CrossRef]
- 31. Shimoda, T.; Juhel, K.; Ampuero, J.-P.; Montagner, J.-P.; Barsuglia, M. Early Earthquake Detection Capabilities of Different Types of Future-Generation Gravity Gradiometers. *Geophys. J. Int.* **2020**, 224, 533–542. [CrossRef]
- 32. Soosalu, H.; Key, J.; White, R.S.; Knox, C.; Einarsson, P.; Jakobsdóttir, S.S. Lower-Crustal Earthquakes Caused by Magma Movement beneath Askja Volcano on the North Iceland Rift. *Bull. Volcanol.* **2010**, 72, 55–62. [CrossRef]
- 33. Zhang, Y.; Chen, S.; Xing, L.; Liu, M.; He, Z. Gravity Changes Before and After the 2008 Mw 7.9 Wenchuan Earthquake at Pixian Absolute Gravity Station in More Than a Decade. *Pure Appl. Geophys.* **2020**, *177*, 121–133. [CrossRef]
- 34. Zhu, Y.; Yang, X.; Liu, F.; Zhao, Y.; Wei, S.; Zhang, G. Progress and Prospect of the Time-Varying Gravity in Earthquake Prediction in the Chinese Mainland. *Front. Earth Sci.* **2023**, *11*, 1124573. [CrossRef]
- 35. Barnes, D.F. Gravity Changes during the Alaska Earthquake. J. Geophys. Res. 1966, 71, 451–456. [CrossRef]
- 36. Fujii, Y. Gravity Change in the Shock Area of the Niigata Earthquake, 16 Jun. 1964. *Zisin J. Seismol. Soc. Jpn. 2nd Ser.* **1966**, 19, 200–216. [CrossRef]
- 37. Hunt, T.M. Gravity Changes Associated with the 1968 Inangahua Earthquake. N. Z. J. Geol. Geophys. 1970, 13, 1050–1051. [CrossRef]
- 38. Kisslinger, C. Processes during the Matsushiro, Japan, Earthquake Swarm as Revealed by Leveling, Gravity, and Spring-Flow Observations. *Geology* **1975**, *3*, 57. [CrossRef]
- 39. Oliver, H.W.; Robbins, S.L.; Grannell, R.B.; Alewine, R.W.; Shawn, B. Surface and Subsurface Movements Determined by Remeasuring Gravity. In *San Fernando*, *California*, *Earthquake of 9 February 1971*; Oakeshott, G.B., Ed.; U.S. Government Printing Office: Sacramento, CA, USA, 1975; pp. 195–211.
- 40. Yun-Tai, C.; Hao-Ding, G.; Zao-Xun, L. Variations of Gravity before and after the Haicheng Earthquake, 1975, and the Tangshan Earthquake, 1976. *Phys. Earth Planet. Inter.* **1979**, *18*, 330–338. [CrossRef]
- 41. Hagiwara, Y. Gravity Changes Resulting from Earthquakes in China. J. Geod. Soc. Jpn. 1979, 25, 10–19. [CrossRef]
- 42. Baldi, P.; Postpischl, D. Gravity Variations during Preseismic Crustal Deformations. *Il Nuovo Cimento C* 1978, 1, 457–464. [CrossRef]
- 43. Lambert, A.; Bower, D.R. Constraints on the Usefulness of Gravimetry for Detecting Precursory Crustal Deformations. *Tectono-physics* **1991**, 193, 369–375. [CrossRef]
- 44. OKUBO, S. Advances in Gravity Analyses for Studying Volcanoes and Earthquakes. *Proc. Jpn. Acad. Ser. B* **2020**, *96*, 50–69. [CrossRef] [PubMed]
- 45. Tanaka, Y.; Kato, A.; Sugano, T.; Fu, G.; Zhang, X.; Furuya, M.; Sun, W.; Okubo, S.; Matsumoto, S.; Honda, M.; et al. Gravity Changes Observed between 2004 and 2009 near the Tokai Slow-Slip Area and Prospects for Detecting Fluid Flow during Future Slow-Slip Events. *Earth Planets Space* 2010, 62, 905–913. [CrossRef]
- 46. Tanaka, Y.; Suzuki, T.; Imanishi, Y.; Okubo, S.; Zhang, X.; Ando, M.; Watanabe, A.; Saka, M.; Kato, C.; Oomori, S.; et al. Temporal Gravity Anomalies Observed in the Tokai Area and a Possible Relationship with Slow Slips. *Earth Planets Space* **2018**, 70, 25. [CrossRef]
- 47. Shahrisvand, M.; Akhoondzadeh, M.; Sharifi, M.A. Detection of Gravity Changes before Powerful Earthquakes in GRACE Satellite Observations. *Ann. Geophys.* **2014**, *57*, A0543. [CrossRef]
- 48. Juhel, K.; Bletery, Q.; Licciardi, A.; Vallée, M.; Hourcade, C.; Michel, T. Fast and Full Characterization of Large Earthquakes from Prompt Elastogravity Signals. *Commun. Earth Environ.* **2024**, *5*, 561. [CrossRef]
- 49. Zhang, S.; Wang, R.; Dahm, T.; Zhou, S.; Heimann, S. Prompt Elasto-Gravity Signals (PEGS) and Their Potential Use in Modern Seismology. *Earth Planet. Sci. Lett.* **2020**, *536*, 116150. [CrossRef]
- 50. Liu, X.; Chen, S.; Xing, H. Gravity Changes Caused by Crustal Fluids Invasion: A Perspective from Finite Element Modeling. *Tectonophysics* **2022**, *833*, 229335. [CrossRef]
- 51. Lough, A.C.; Wiens, D.A.; Nyblade, A. Reactivation of Ancient Antarctic Rift Zones by Intraplate Seismicity. *Nat. Geosci.* **2018**, *11*, 515–519. [CrossRef]
- 52. Rubin, A.M. Propagation of Magma-Filled Cracks. Annu. Rev. Earth Planet. Sci. 1995, 23, 287–336. [CrossRef]
- 53. Rymer, H.; Brown, G. Gravity Fields and the Interpretation of Volcanic Structures: Geological Discrimination and Temporal Evolution. *J. Volcanol. Geotherm. Res.* **1986**, 27, 229–254. [CrossRef]

Appl. Sci. 2025, 15, 11126 26 of 26

54. Chariskou, C.; Vrochidou, E.; Daniels, A.J.; Kaburlasos, V.G. Variable Selection on Reflectance NIR Spectra for the Prediction of TSS in Intact Berries of Thompson Seedless Grapes. *Agronomy* **2022**, *12*, 2113. [CrossRef]

- 55. Govers, R.; Furlong, K.P.; van de Wiel, L.; Herman, M.W.; Broerse, T. The Geodetic Signature of the Earthquake Cycle at Subduction Zones: Model Constraints on the Deep Processes. *Rev. Geophys.* **2018**, *56*, 6–49. [CrossRef]
- 56. McKenzie, D. Active Tectonics of the Mediterranean Region. Geophys. J. Int. 1972, 30, 109–185. [CrossRef]
- 57. Papazachos, B.C.; Papadimitriou, E.E.; Kiratzi, A.A.; Papazachos, C.B.; Louvari, E.K. Fault Plane Solutions in the Aegean Sea and the Surrounding Area and Their Tectonic Implication. *Boll. Geofis. Teor. Appl.* **1998**, *39*, 199–218.
- 58. Shaw, B.; Jackson, J. Earthquake Mechanisms and Active Tectonics of the Hellenic Subduction Zone. *Geophys. J. Int.* **2010**, *181*, 966–984. [CrossRef]
- 59. Herak, M. Conversion between the Local Magnitude (ML) and the Moment Magnitude (Mw) for Earthquakes in the Croatian Earthquake Catalogue. *Geofizika* **2020**, *37*, 197–211. [CrossRef]
- 60. Scordilis, E.M. Empirical Global Relations Converting M S and m b to Moment Magnitude. J. Seismol. 2006, 10, 225–236. [CrossRef]
- 61. Frankel, A.D.; Mueller, C.S.; Barnhard, T.P.; Leyendecker, E.V.; Wesson, R.L.; Harmsen, S.C.; Klein, F.W.; Perkins, D.M.; Dickman, N.C.; Hanson, S.L.; et al. USGS National Seismic Hazard Maps. *Earthq. Spectra* **2000**, *16*, 1–19. [CrossRef]
- 62. U.S. Department of the Interior Earthquake Hazards Program. Available online: https://www.usgs.gov/programs/earthquake-hazards (accessed on 25 August 2025).
- 63. GFZ Helmholtz Centre for Geosciences GFZ Data Services. Available online: https://dataservices.gfz-potsdam.de/web/(accessed on 25 August 2025).
- 64. COST-G Team International Combination Service for Time-Variable Gravity Fields (COST-G). Available online: https://cost-g.org/(accessed on 25 August 2025).
- 65. Calandra, S.; Teti, D. Correlation Study: Triggering and Magnitude of Earthquakes in Italy (≥M4. 3) in Relation to the Positions and Gravitational Forces of the Sun, Moon, and Planets Relative to Earth. *New Concepts Glob. Tecton. J.* **2024**, *12*, 1–26.
- 66. Mahmud, S. The Combined Effects of the Gravitational Forces on the Tectonic Plates on Earth's Surface Exerted by the Moon, the Sun and the Other Planets Are One of the Main Reasons of the Earthquakes. *Int. J. Adv. Res. Phys. Sci.* **2019**, *6*, 44–62.
- 67. Romanet, P. Could Planet/Sun Conjunctions Be Used to Predict Large (Moment Magnitude ≥ 7) Earthquakes? *Seismica* **2023**, 2, 1–6. [CrossRef]
- 68. Senapati, B.; Kundu, B.; Jha, B.; Jin, S. Gravity-Induced Seismicity Modulation on Planetary Bodies and Their Natural Satellites. *Sci. Rep.* **2024**, *14*, 2311. [CrossRef] [PubMed]
- 69. Straser, V. Variations in Gravitational Field, Tidal Force, Electromagnetic Waves and Earthquakes. *New Concepts Glob. Tecton. Newsl.* **2010**, *57*, 98–108.
- 70. Neumeyer, J.; Hagedoorn, J.; Leitloff, J.; Schmidt, T. Gravity Reduction with Three-Dimensional Atmospheric Pressure Data for Precise Ground Gravity Measurements. *J. Geodyn.* **2004**, *38*, 437–450. [CrossRef]
- 71. Rabbel, W.; Zschau, J. Static Deformations and Gravity Changes at the Earth's Surface Due to Atmospheric Loading. *J. Geophys. Z. Geophys.* **1985**, *56*, 81–89.
- 72. Namias, J. Summer Earthquakes in Southern California Related to Pressure Patterns at Sea Level and Aloft. *J. Geophys. Res. Solid. Earth* **1989**, 94, 17671–17679. [CrossRef]
- 73. Hasan, S.; Troch, P.A.; Boll, J.; Kroner, C. Modeling the Hydrological Effect on Local Gravity at Moxa, Germany. *J. Hydrometeorol.* **2006**, *7*, 346–354. [CrossRef]
- 74. Zhang, M.; Liu, Z.; Wu, Q.; Teng, Y.; Zhang, X.; Du, F.; Jiang, Y. Hydrologic Changes of In-Situ Gravimetry. *Geophysics* **2022**, *87*, B117–B127. [CrossRef]
- 75. Bragato, P.L. Statistical Relationship Between the Decrease of Major Seismicity and Drought in Southern California Since 1900. *Front. Earth Sci.* **2021**, *9*, 790412. [CrossRef]
- 76. Johnson, C.W.; Fu, Y.; Bürgmann, R. Stress Models of the Annual Hydrospheric, Atmospheric, Thermal, and Tidal Loading Cycles on California Faults: Perturbation of Background Stress and Changes in Seismicity. *J. Geophys. Res. Solid. Earth* **2017**, 122, 605–625. [CrossRef]
- 77. Simon, V.; Kraft, T.; Maréchal, J.-C.; Helmstetter, A.; Diehl, T. Climate-Change-Induced Seismicity: The Recent Onset of Seasonal Microseismicity at the Grandes Jorasses, Mont Blanc Massif, France/Italy. *Earth Planet. Sci. Lett.* **2025**, *666*, 119372. [CrossRef]
- 78. Kreemer, C.; Zaliapin, I. Spatiotemporal Correlation Between Seasonal Variations in Seismicity and Horizontal Dilatational Strain in California. *Geophys. Res. Lett.* **2018**, *45*, 9559–9568. [CrossRef]

Disclaimer/Publisher's Note: The statements, opinions and data contained in all publications are solely those of the individual author(s) and contributor(s) and not of MDPI and/or the editor(s). MDPI and/or the editor(s) disclaim responsibility for any injury to people or property resulting from any ideas, methods, instructions or products referred to in the content.